Hydration Kinetics and Performance of Sodium Carbonate-Activated Slag-Based Systems Containing Reactive MgO and Metakaolin under Carbonation

Busra Akturk[1], Mehrnosh Abolfathi[2], Serhan Ulukaya[3], Ahmet B. Kizilkanat[4], Thomas J. N. Hooper[5], Lei Gu[6], En-Hua Yang[7], Cise Unluer[8]

[1*]Istanbul Bilgi University, Civil Engineering Department, 34060, Istanbul, Turkey, E-mail: busra.akturk@bilgi.edu.tr (*Corresponding author)

[2] Yildiz Technical University, Civil Engineering Department, 34220, Istanbul, Turkey, E-mail: mehrnoshabolf@gmail.com

[3] Yildiz Technical University, Civil Engineering Department, 34220, Istanbul, Turkey, E-mail: serhanu@yildiz.edu.tr

[4] Aksoy St. No:3/3, 34145, Istanbul, Turkey, E-mail: ahmet.kizilkanat@gmail.com

[5] NTU Centre of High-Field NMR Spectroscopy and Imaging, School of Physical and Mathematical Sciences, Nanyang Technological University, 21 Nanyang Link, 637371, Singapore, E-mail: thooper@ntu.edu.sg

[6] School of Civil and Environmental Engineering, Nanyang Technological University, 50 Nanyang Avenue, Singapore 639798, Singapore, E-mail: lei.gu@ntu.edu.sg

[7] School of Civil and Environmental Engineering, Nanyang Technological University, 50 Nanyang Avenue, Singapore 639798, Singapore, E-mail: ehyang@ntu.edu.sg

[8] School of Engineering, University of Glasgow, G12 8LT, Glasgow, United Kingdom, E-mail: Cise.Unluer@glasgow.ac.uk

ABSTRACT

The hydration mechanism and strength development of sodium carbonate-activated slag-based systems mainly depend on the additives used. Although the effects of mineral additives in such systems have been extensively investigated, the effects of Mg^{2+}, Al^{3+}, and Si^{4+} ions increasing with the addition of reactive MgO (Mg) and metakaolin (Mk) on the hydration mechanism of such systems have not been established yet. This study investigated the hydration kinetics and performance of sodium carbonate-activated ternary blended slag-based binder systems. The hydration mechanism was revealed by isothermal calorimetry and mechanical performance was evaluated with the measurement of compressive strength at different ages up to 56 days. The reaction mechanisms were investigated through X-ray diffraction, Fourier transform infrared spectroscopy, thermogravimetric analysis and ^{29}Si and ^{27}Al solid-state nuclear magnetic resonance (NMR). C-(A)-S-H, Na and Al-enriched C-(N,A)-S-H and hydrotalcite were the main reaction products responsible for the strength development of the samples, accompanied by the minor contribution of other carbonate-containing phases. Partial replacement of slag with Mg and Mk led to high early-age strengths compared to plain samples when Mk was used at 5%. Samples incorporating Mg and Mk achieved similar or higher strengths than ordinary Portland cement-based samples. However, an increase in replacement ratio of Mk beyond 5% led to a significant decrease in compressive strength. Furthermore, the performance of samples under accelerated carbonation was studied. The use of Mg and Mk enhanced carbonation resistance due to enhanced hydrotalcite and C-(N,A)-S-H gel formation, highlighting the potential of using slag-Mg-Mk blends as an alternative binder system.

Keywords: Sodium carbonate activation; reactive MgO; metakaolin; slag; microstructure; accelerated carbonation.

1. Introduction

Portland cement (PC) production causes a high amount of CO_2 emissions and increases energy demand. The output of PC obtained from the calcination of limestone and clay minerals at high temperatures (~1400°C in a kiln) emits approximately one tonne of CO_2 per tonne of produced PC, making it is responsible for 7-9% of global CO_2 emissions [1]. Efforts have been made to reduce CO_2 emissions through the development of new concrete technologies with cement-free solutions. Currently, there are two options that are being investigated. One is the partial replacement of PC used in concrete production with pozzolanic by-products such as ground granulated blast furnace slag and fly ash. The other is the preparation of an aqueous solution to be constituted by an alkali silicate, hydroxide, sulphate, carbonate, or mixture. A mixture of any raw material containing reactive aluminosilicate within these solutions provides alkali-activated materials (AAM) and geopolymers [2]. AAM can be a promising alternative eco-friendly material since they contain industrial wastes and/or natural pozzolans, such as fly ash, blast furnace slag, metakaolin, and pumice powder as a binder.

Most previous studies focused on using alkali silicates and alkali hydroxides as activators [3–8]. However, these activators cause considerable energy consumption during the manufacturing processes, limiting sustainability. Additionally, the produced materials may face some unwanted issues such as high drying shrinkage, rapid setting, and micro-cracking [9,10]. As an alternative to these systems, the use of sodium carbonate (Na_2CO_3) as an activator may be a more cost-effective, environmentally friendly and less caustic with a lower drying shrinkage. Despite the advantages that sodium carbonate (NC)-activation offers, a limited number of studies were reported in alkali-activated systems, mainly due to drawbacks such as prolonged setting time and low compressive strength at early ages [11,12]. It was reported that alkaline hydroxides/silicates-activated slag hardened within three hours and gained a 7-day compressive strength higher than 40 MPa. Whereas, NC-activated slag systems have required an extended setting of up to three days, with a lower compressive strength of about 15 MPa [13,14]. However, NC-activated systems have shown higher strength at longer ages than sodium hydroxide-activated systems due to the contributing effect of carbonate compounds [15,16].

In NC-activated systems, the reaction occurs when the pH value exceeds the lower limit level (>12), initiating slag dissolution. As a result of the preferential reaction between Ca^{2+} from slag and CO_3^{2-} from NC, carbonate compounds such as calcite and gaylussite form. Unfortunately, calcite and gaylussite do not provide a high degree of cohesion to develop high early strength. Because of the slow dissolution mechanism of slag under the lower pH induced by NC, the reaction proceeds gradually. Once the CO_3^{2-} is exhausted, hydroxide ions are released, which increase the pH, leading to the dissolution of silicate species and formation of the strength-giving C-(A)-S-H phase, thus, expediting the reaction [17–20].

Several studies have focused on accelerating the setting time and improving the early age strength of NC-activated slag systems with several additives like PC, CaO, and reactive MgO or secondary activators such as sodium hydroxide (NH) and sodium silicate, giving higher pH values [14,21–25]. One of these attempts reported by Akturk et al. [20], replaced NC with NH at different ratios (20% and 40% by weight) and incorporated calcium hydroxide to reduce the setting time and enhance the compressive strength to desirable levels. These mixes hardened within approximately 6 hours and had higher early-age strengths (i.e. 20 MPa at day 3) when compared with the other AAM systems. Ke et al. [18] used layered double hydroxide (CLDH) since CLDH removes carbonate anion from the medium, yielding a significant increase in the

pH and enhancing dissolution of slag. However, the use of CLDH may not be a sustainable approach since the production of CLDH requires a significant amount of energy [18,26,27].

Several studies reported that reactive MgO could be regarded as an alternative activator for the activation of slag [28]. Reactive MgO is produced at low calcination temperatures at about 700°C [29,30], which also results in CO_2 emissions, unless obtained from alternative sources such as desalination reject brine [31,32]. Incorporating reactive MgO creates hydrotalcite-like phases as a result of its hydration, contributing to higher strength and lower shrinkage in alkali-activated slag systems [28,33,34]. At the beginning of the reaction, reactive MgO dissolves in water and provides an alkaline environment, which causes the breaking of Si-O-Si and Al-O-Si bonds. The broken Si-O and Al-O bonds react with the Mg^{2+} ion to form magnesium silicate hydrate (M-S-H) and hydrotalcite ($Mg_6Al_2(CO_3)(OH)_{16}.4(H_2O)$) [34]. MgO increases the pH level of the medium, which can expedite the dissolution of slag, thus accelerating the reaction [35–37]. It was indicated that the CaO content and degree of reactivity of the reactive MgO are the two main factors in the dissolution of slag [34,38]. It was also revealed that the MgO plays a role in slag dissolution since it controls the secondary products such as hydrotalcite depending on the amount of available Al^{3+} ion in the systems [39].

Metakaolin (Mk) is one of the most studied raw materials as an aluminosilicate source in AAM production. The main hydration products of metakaolin-based systems are three-dimensional zeolite-like polymers and aluminosilicate oligomers, and sodium aluminium silicate hydrate gels, which transform into zeolite at later ages in NH-activated systems [40]. Many studies have been carried out on NH or sodium silicate-activated metakaolin and metakaolin/slag blend systems [41–44]; however, no research has been found on the activation of NC. Previous studies of systems using metakaolin as the raw material, showed that Al or Na-enriched phases and C-S-H gel were formed by the additional dissolved Al^{3+} and Na^{+} ions. The incorporation of a low amount of metakaolin into the slag systems enhances the early-age strength and promotes workability. However, after a specific ratio, the increased metakaolin content reduces compressive strength at later ages due to the incomplete reaction of incorporated metakaolin [41–44].

The studies mentioned above mainly focused on accelerating the hydration mechanism of NC-activated slag by incorporating different reactive additives. Several studies investigated and compared the effect of reactive MgO on the strength development and microstructure of NC-activated slag. Only a few studies have reported the effect of metakaolin incorporation on alkali-activated slag-based systems [42,45–49]. Furthermore, the effects of both reactive MgO and metakaolin in NC-activated systems have not been studied until now. This gap in the literature could be critical as with the incorporation of MgO and metakaolin, additional Mg^{2+}, Al^{3+}, and Si^{4+} ions can accelerate the reaction mechanisms, improve workability and enhance the early age strength.

AAMs are known to have superior durability against chloride penetration, chemicals, and freezing/thawing cycles [50–56]. However, they are vulnerable to carbonation, during which the diffused CO_2 results in the reduction of the pH in the pore solution, causing decalcification of C-(A)-S-H. While previous studies generally focused on the carbonation behaviour of slag or fly ash-based systems, only few have revealed the effect of Mg incorporation in the system. However, the effect of both Mg and Mk, as an aluminosilicate source, on slag-based systems under accelerated carbonation is yet to be investigated systematically.

Considering this gap in the literature, this paper presents a comprehensive analysis of the combined use of reactive MgO (Mg) and metakaolin (Mk) to improve the reaction kinetics, performance, and carbonation resistance of NC-activated slag-based systems. The influence of these two additives (Mg and Mk) on the hydration kinetics and microstructure were analysed on paste samples by isothermal calorimetry, X-ray diffraction analysis (XRD), Fourier transform infrared spectrometry (FTIR), ^{29}Si and ^{27}Al solid-state nuclear magnetic resonance (NMR), and thermogravimetry-differential thermogravimetry (TG-DTG). The mechanical performance of NC-activated slag-based mortar samples was analysed by compressive strength measurements at different ages. Furthermore, the carbonation resistance of these mortar mixes was evaluated under an accelerated carbonation environment. SEM-EDS analysis was also performed to investigate the morphology and examine the formation of hydration products of the paste samples.

2. Materials and Methodology

2.1 Materials and mix proportions

Ground granulated blast furnace slag, obtained from Eregli Iron and Steel Factory, Turkey, was used as a main binder in this study. Reactive MgO, supplied by KUMAS Magnesia Company, Turkey, which was produced by lightly calcining $MgCO_3$ at approximately 750°C, was used as one of the secondary binders. Metakaolin, obtained from Kaolin EAD Company, Bulgaria, was used as the aluminosilicate precursor. CEM I 42.5 R type ordinary Portland cement was used in the series produced for comparison purposes. Table 1 presents the chemical compositions and the physical properties of the raw materials that were determined by X-ray fluorescence.

Table 1. Chemical composition and physical properties of slag, reactive MgO, metakaolin, and cement.

Chemical composition (%) by wt.	Slag	MgO	Metakaolin	PC
SiO_2	36.6	6.0	56.1	18.9
Al_2O_3	14.2	0.7	40.3	4.8
Fe_2O_3	1.0	0.3	0.9	3.3
CaO	34.8	3.3	0.2	63.7
MgO	8.3	83.6	0.2	1.5
SO_3	0.9	0.2	–	3.3
Cl^-	<0.1	–	–	<0.1
Na_2O	0.4	0.4	0.2	0.4
K_2O	0.7	–	0.6	0.7
TiO_2	1.0	–	0.6	–
LOI (%)	–		1.1	2.9
Specific surface area (m^2/g)	0.27	0.19	0.32	0.39
Specific gravity	2.88	3.55	2.30	3.10

To produce mortar samples, siliceous-based sand with a specific gravity of 2.67 was used as a fine aggregate and its ratio was kept constant at 50% by volume. The particle size distributions of sand, slag, Mg, and Mk, which were obtained by Mastersizer analysis, are shown in Fig. 1. The particle size range of slag, Mk, and Mg were 0.4–30 μm, 0.4–30 μm, and 0.4–200 μm; with a mean (d_{50}) of about 9 μm, 3 μm, and 23 μm, respectively.

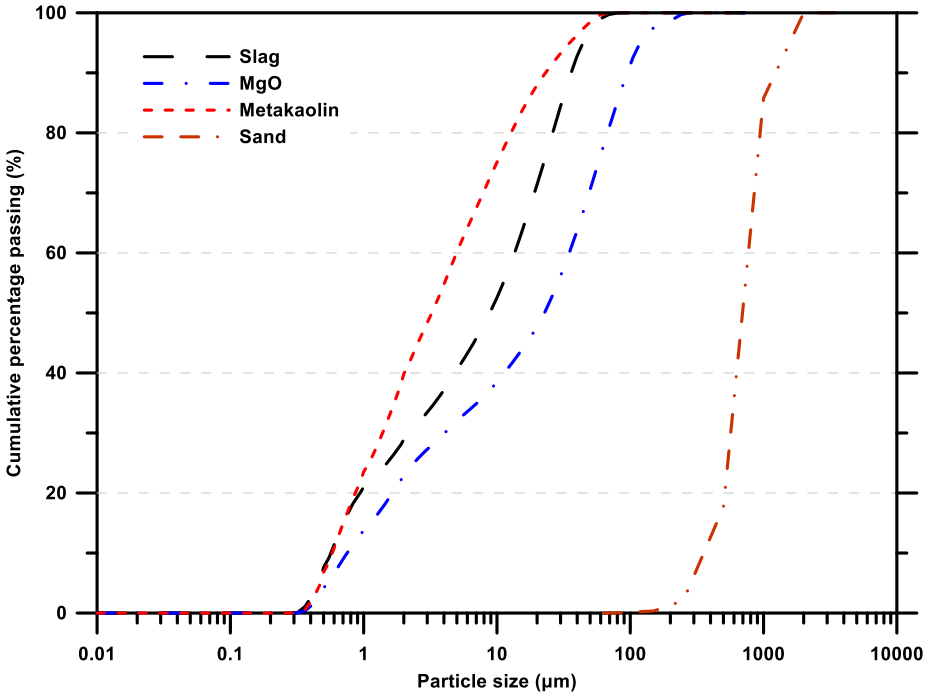

Fig. 1. Particle size distribution of slag, reactive MgO, metakaolin and sand.

The mineralogical phases of slag, Mg, and Mk, expressed by X-ray diffractometer patterns, are shown in Fig. 2. Slag revealed an amorphous hump over a 2θ range of 23° and 35°, and no pronounced peaks were observed in the related pattern. This hump represented the crystalline and glassy portion of the sample, which indicated a gehlenite-like mineral. The prominent peaks of Mg were observed at 42.9° 2θ and 62.3° 2θ which were identified as periclase, along with brucite at 38° 2θ. One primary and one small quartz peaks were observed in Mk (Fig. 2).

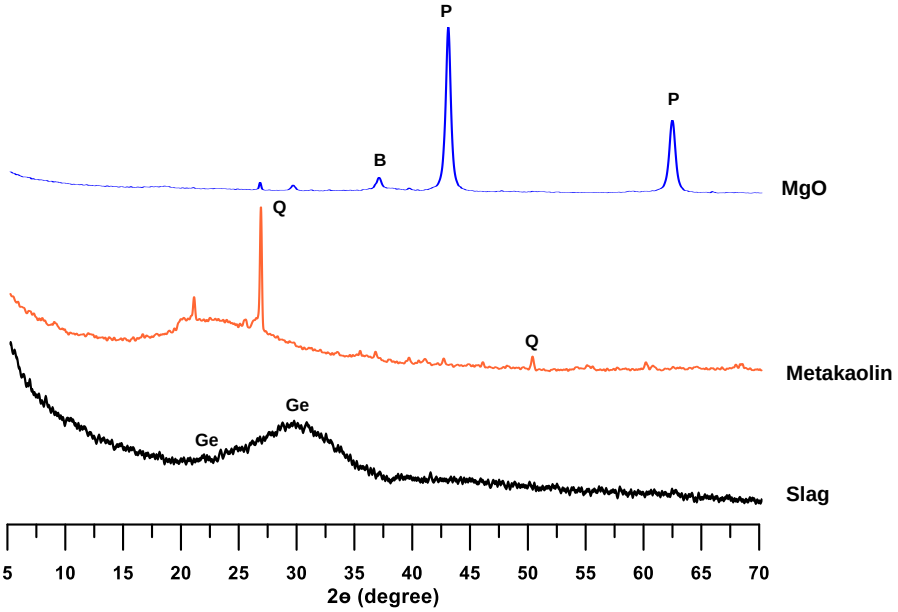

Fig. 2. XRD patterns of slag, reactive MgO, and metakaolin (Ge: Gehlenite; Q: Quartz; B: Brucite; P: Periclase).

Four different paste and mortar mixes containing different amounts of Mg and Mk were prepared to determine the compressive strength and microstructural properties. Mixes were

coded as shown in Table 2, where the 100S refers to reference mix containing 100% of the main binder, slag. For other combinations, the denotation of the blends comprises Mg and Mk; the first number refers to Mg and the second one refers to Mk percentages in the total binder, respectively. For example, 5Mg10Mk means the mix was prepared by substituting slag with 5% of Mg and 10% of Mk.

The water to binder ratio was set at 0.35 for paste samples and 0.45 for mortar samples. Analytical grades of NC was used as an activator, and concentration was kept constant at 10% by mass of the total binder, which corresponded to approximately 6% of Na_2O. Although one-part alkali-activated slag-based binders have preferable characteristics in terms of safety and ease of handling, the ordinary (two-part) mixing procedure was adopted due to several drawbacks of the former such as prolonged setting time, higher porosity and reduction in ultimate strength [57]. Therefore, before proceeding to the mixing step, NC was dissolved in water to prepare an activator solution. Raw materials were mixed in a benchtop mixer to achieve homogeneity and then cast into conical falcon tubes with a volume of 50 ml for paste samples. Mortar specimens were produced to determine the compressive strength of mixes, and the prepared mixture was cast into 50 × 50 × 50 mm cubic molds for the mortars. Immediately after the casting, the cubic molds were covered with a plastic sheet to prevent moisture exchange during the curing period.

Table 2. Compositions of mortar samples.

Mixes	Binder types and percentages by weight			Water/ Binder	Amount of constituents (kg/m^3)					
	Slag	MgO	Metakaolin		Slag	MgO	Metakaolin	Na_2CO_3	Sand	Water
100S	100	-	-	0.45	600	-	-	60	1335	270
5Mg10Mk	85	5	10		510	30	60			
10Mg	90	10	-		540	60	-			
10Mg5Mk	85	10	5		510	60	30			

Once the samples were produced, they were separated into two groups as non-carbonated and accelerated carbonated. The first group of samples was kept under laboratory conditions at 23 ± 2°C, with a relative humidity of 65 ± 5% for the first 24 hours. Then, all samples were exposed to high temperature curing at 60°C in a drying oven for additional 24 hours, followed by the same laboratory conditions until the testing day. For the sample group to be exposed to accelerated carbonation, after the high-temperature curing, they were placed in a carbonation chamber having 10% of CO_2 concentration and 65 ± 5% relative humidity and kept until the testing day, i.e., 56 days. Both paste and mortar samples were cured under the same conditions as described above.

2.2 Methodology

2.2.1 Isothermal calorimetry

The heat flow and cumulative heat evolved corresponding to the hydration of Mg and Mk incorporated NC-activated slag-based paste mixes were studied at 30°C by an I-Cal 2000 High Precision Calorimeter, as per ASTM C1702 [58]. To prepare the paste samples, all materials were heated to 30°C to produce mixes at the same temperature as the measurement temperature. The ready-mix was instantaneously placed into the isothermal calorimeter channel to measure the heat of hydration. The heat flow was recorded for the first 72 hours of reaction.

2.2.3 pH

The pH values of the paste samples were determined on crushed and ground samples, passing through a 75 μm sieve size. The ground paste samples were dispersed in distilled water at a ratio of 1:5 and mixed for 15 min at 1000 rpm by a magnetic stirrer. The obtained solution was filtered and the pH measurement was recorded by a *Hanna* pH meter with an accuracy of ±0.01. The pH values of each paste sample were taken at definite times (e.g. 1, 3, 6, 12 and 24 hours), up to 72 hours of reaction.

2.2.3 Compressive strength

The compressive strength of mortar mixes was determined by following ASTM C109 [59]. The measurements were performed at 3, 7, 28, and 56 days for the first group samples exposed to the laboratory conditions. The compressive strength of the second group of samples stored in a carbonation chamber was also measured on 56^{th} day. A loading rate of 1.5 kN/s was applied in the compression tests and an average of three test results was reported for each mix.

2.2.4 X-ray diffraction

The X-ray diffraction (XRD) analysis was used for the identification of the hydration products of two groups of samples; cured in the laboratory environment (non-carbonated group) and exposed to accelerated carbonation (carbonated group). The analysis was performed at 56 days for both environment condition and accelerated carbonated group samples. The paste samples were crushed and dried at 60°C for 24 h, followed by passing a sieve with a size of 75 μm. The fine powders were analysed using an XPERT-PRO X-ray diffractometer analyzer with CuKα radiation. The samples were step-scanned from 5° 2θ to 65° 2θ at a step size of 0.02° 2θ and a measuring time of 1 s/step.

2.2.5 Fourier transform infrared spectroscopy

Fourier transformed infrared spectroscopy (FTIR) data recorded using a Perkin Elmer Spectrum 100 Spectrometer. The spectra was acquired with 32 scans from 4000 to 400 cm^{-1} per spectrum. The band between 600 cm^{-1} and 2100 cm^{-1} was only considered for analyzing the results since the reaction products were appeared at this range. FTIR analysis was used to identify and interpret the hydration products for 56 days of curing under environment conditions and after exposure to accelerated carbonation.

2.2.6 Thermogravimetric analysis

Thermogravimetric and derived thermogravimetric analyses (TG-DTG) were performed using EXSTAR 6000 thermal analyzer. The temperature scanning range was set from 25°C to 900°C and increased with the heating rate of 15°C/min under nitrogen flow. About 20-25 mg powder of the paste samples were used and TG-DTG analysis were conducted at the curing age of 56 days for both two non-carbonated and carbonated paste samples. The mass loss at different temperature ranges was used to quantify the amounts of reaction products.

2.2.7 Solid-state NMR

Solid-state NMR experiments were performed on non-carbonated and carbonated paste powder samples, which had undergone 56 days of curing. All solid-state NMR experiments were completed on a 14.1 T Bruker Advance III HD 600 MHz spectrometer. All spectra were processed using the Topspin software package and referenced to the unified scale using IUPAC recommended frequency ratios relative to the ^{13}C adamantane$_{(s)}$ methylene resonance (δ = 37.77 ppm) [60,61]. Spectral deconvolution was performed with dmfit [62]. The ^{27}Al ($\upsilon_0(^{27}Al)$ = 156.35 MHz) and ^{29}Si ($\upsilon_0(^{29}Si)$ = 119.23 MHz) NMR experiments were acquired using a 4 mm Bruker HXY probe at an MAS frequency of 14 kHz. The ^{27}Al NMR one-pulse sequence utilised a selective $\pi/6$ pulse of 1 μs (determined on yttrium aluminium garnet$_{(s)}$) and a 0.1 s recycle delay. The ^{29}Si NMR one-pulse sequence utilised a non-selective $\pi/2$ pulse of 5.3 μs (determined on kaolinite$_{(s)}$) and a 300 s recycle delay.

2.2.8 SEM-EDS

Scanning electron microscope (SEM) combined with Energy dispersive X-ray spectroscopy (EDS) was performed on the ZEISS EVO LS10 machine at an accelerating voltage of 15 kV. All samples are tested at the 56th days of the reaction. Secondary and backscattered electron images were taken to determine the hydration products and display the area fraction of the hydrated phase and unhydrated slag particles, representing the influence of secondary binders on the hydration degree both under environmental and carbonated conditions. Secondary electron imaging was used to determine the morphology and hydration products in non-carbonated and carbonated mixes. Several points on the paste samples were picked for the determination of its elemental composition. The backscattered images (BSE) were used to determine the unhydrated slag particles and gel structure of mixes and were collected at different magnifications such as 1000×, 2500×, and 5000×.

3. Results and Discussion

3.1 Isothermal calorimetry

The heat flow associated with the hydration of the Mg and Mk containing NC-activated slag-based pastes over 60 h are shown in Fig. 3. It can be seen from Fig. 3(a) that the dissolution of the precursor was detected shortly after mixing in all the samples. The heat flow curves during the first few hours indicated that the hydration of 10Mg and 10Mg5Mk samples was faster than 100S sample, whereas the hydration of 5Mg10Mk sample was slower than 100S sample. This observation confirmed the beneficial role of Mg played in the dissolution of slag [36], whereas the addition of high amount of Mk potentially slowed down the initial hydration. The second exothermic peaks were observed after around 5 h in all samples due to the hydration of slag [20]. After around 8 h of hydration, the heat flow of 100S, 10Mg, and 10Mg5Mk samples gradually reduced, whereas the heat flow of 5Mg10Mk sample increased slightly with a third exothermic peak after around 20 h of hydration. This observation indicated that the initial hydration of 5Mg10Mk sample was delayed, potentially due to the high amount of Mk.

It can be seen from the cumulative heat curves in Fig. 3(b) that the highest hydration degree was revealed by 10Mg sample, followed by 10Mg5Mk sample. Both of the 10Mg and 10Mg5Mk samples showed higher cumulative heat flow than 100S sample, indicating that the

introduction of 10% MgO in the binder significantly increased the overall hydration process. 5Mg10Mk sample showed the lowest cumulative heat flow, revealing the adverse effect of 10% Mk use on the overall hydration process. However, in spite of the delayed hydration observed in 5Mg10Mk in Fig. 3(a), its cumulative heat flow gradually approached 100S sample after 60 h of hydration.

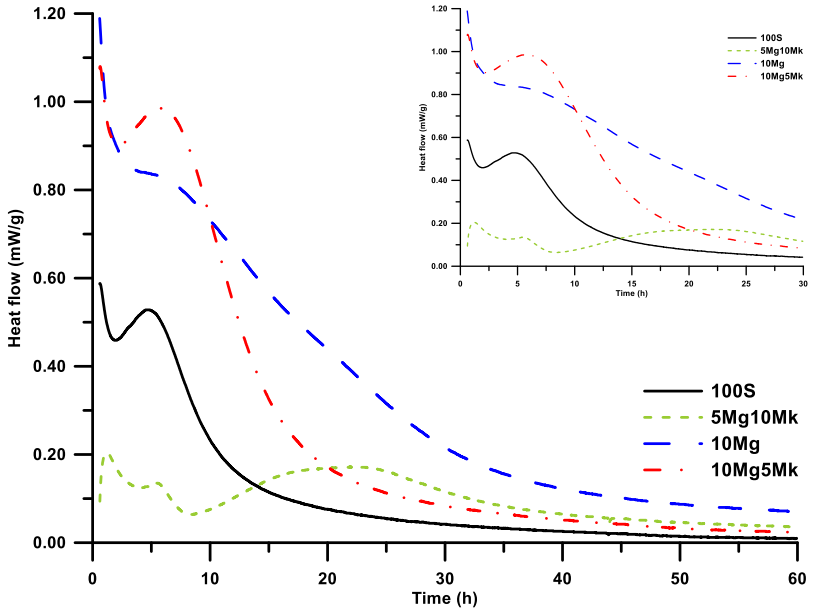

(a)

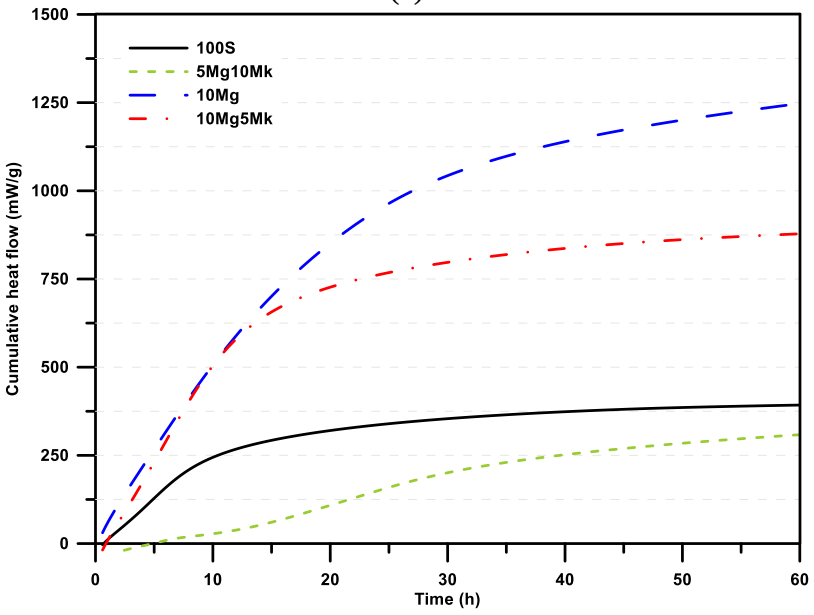

(b)

Fig. 3. Isothermal calorimetry results of pastes showing the (a) heat flow and (b) cumulative heat.

3.2 pH

The pH values of all paste samples are shown in Fig. 4. The initial pH values obtained during the first hour ranged between 12.20 and 12.39, which then increased over time and reached the maximum values at 24 hours, subsequently decreasing at 48 and 72 hours. The pH values of

10Mg and 10Mg5Mk mixes were higher than that of the control sample, 100S, at all measurement times. The presence of Mg ions resulted in higher values in the pH of the fresh pastes, which was attributed to the increased dissolution of MgO, led to the formation of hydrotalcite. Removing a higher amount of carbonates from the medium caused higher dissolution of slag, continuing with further Ca^{2+} release. On the other hand, 5Mg10Mk represented lower values than other Mg and Mg+Mk containing mixes, especially for the first hours of the reaction. The lower pH values of 5Mg10Mk mixes corroborated with the isothermal calorimetry results, which could explain their delayed hydration mechanism.

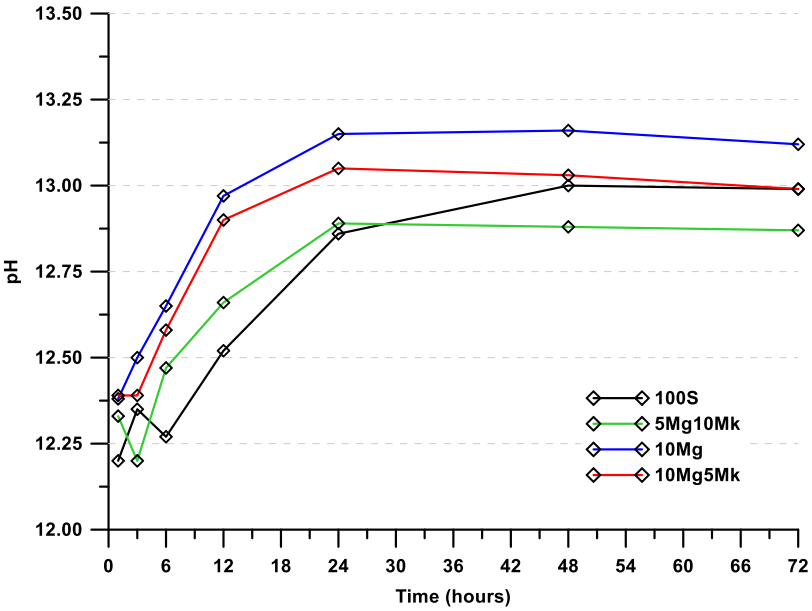

Fig. 4. pH values during the first 72 hours of reaction.

3.3 Compressive strength

3.3.1 Effect of secondary binders on compressive strength

Fig. 5 exhibits the compressive strength development of NC-activated ternary blend slag-based mortar mixes up to 56 days of curing. It can be observed that all NC-activated mixes, except 5Mg10Mk, reached at least 47 MPa for the 3-days strength, which was higher than the cement-based mix. In line with the reaction kinetics, the substitution of Mg and Mk in the prepared mixes led to a slight improvement in the early age compressive strength compared with the cement-free control sample 100S. 10Mg5Mk mortar reached approximately 52 MPa at 3 days, exceeding the strength of cement-based mixes, e.g., 40.7 MPa. The higher early strength in 10Mg and 10Mg5Mk mixes are associated with the formation of hydrotalcite by the additional amount of Mg^{2+} and Al^{3+} ions in the system by incorporating Mg and Mk. On the other hand, Mg and Mk substitution did not enhance the final strength, i.e., at 56 days.

Except for the 5Mg10Mk mix, all NC-activated mixes presented similar strength values ranging between 50-55 MPa and 60–63 MPa at 28 and 56 days, respectively. The maximum strength value obtained in Mg-substituted 10Mg mixes, which can be attributed to the formation of hydrotalcite demonstrated by XRD analysis (Fig. 7). Several studies investigated the compressive strength of alkali-activated blend systems and found that the blends present higher compressive strength than the mixes containing only one precursor. Bignozzi et al. [63] reported

that with the incorporation of metakaolin into the alkali-activated electric arc furnace and ladle slag, the compressive strength increased. Yang et al. [64] reported that substitution of fly ash with metakaolin leads to higher compressive strength since metakaolin decreases the average reactivity of the solid precursors, which results in prolongation of the polymerization stage and this promotes densification of binding gels prior to hardening and then a more compact N-(A)-S-H gel is formed with lower Al/Si ratio. Fernandez-Jimenez et al. [65] revealed that blend of fly ash and metakaolin presents higher strength than the mix containing only metakaolin. The reason for this increase was attributed to the increase in the gel/zeolite ratio and the higher Si/Al ratio in the gel structure.

Contrary to the enhanced compressive strength in 10 Mg and 10Mg5Mk mixes, with the higher portion of the 15% total replacement ratio being made with metakaolin, that is, an increase in the Mk content to 10% caused a tremendous decrease in the compressive strength for all test days (Fig. 5). 5Mg10Mk mix reached only 1.2 MPa after 56 days of curing, which can be inferred that this type of mortar is not appropriate to be used for structural purposes. The reason for this abruptly low strength value is explained in the microstructure analysis. Bernal et al. [66] studied the effects of incorporation of Mk on alkali silicate-activated slags. The authors reported that up to 20% substitution of Mk with slag caused significant reductions in the compressive strength, suggesting that the alkalinity of the system may not be high enough for dissolution of metakaolin. Another study [67] stated that the compressive strength of alkali silicate-activated slag/metakaolin blends show differences in compressive strength performance depending on the amount of Mk and activator modulus. Stevenson and Sagoe-Crastil [68] studied the activation of metakaolin-based alkali silicates and hydroxides-activated systems. They revealed that compressive strength depends on the Si/Al ratio in the mix and higher ratios give higher strength values. In contrast to previously mentioned studies, Bernal et al. [44] found that the reactivity of metakaolin depends on the activator concentration used and thus the alkalinity of the system. They reported that an increase in the activator concentration as the metakaolin increase favoured the reaction of Mk without hindering the dissolution of Ca^{2+}. The higher alkalinity promotes the dissolution of the Si and Al species from the Mk at high activator concentrations; the alkalinity is reduced by the deprotonation of hydrated silica molecules and the consumption of Na by the formation of aluminosilicate hydration products. So, the release of Ca^{2+} from the slag becomes less restricted.

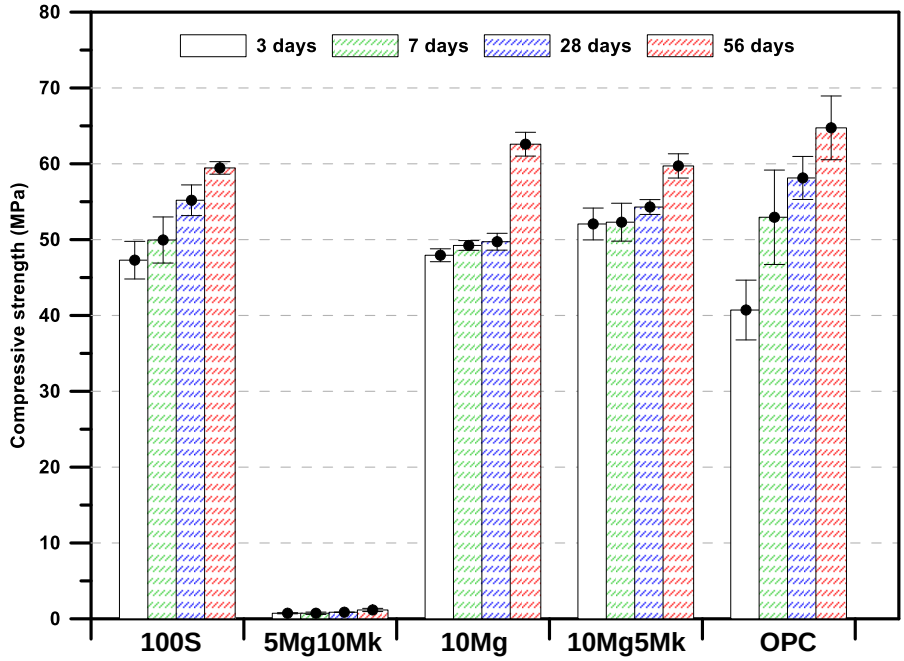

Fig. 5. Compressive strength values of all mixes at 3, 7, 28 and 56 days.

It was observed that there is a gradual increase for the control mix (100S) and cement-based mix over time. On the other hand, when the time-dependent compressive strength developments of Mg and Mk incorporated mixes are analyzed, it is seen that there are no significant changes in strength values until the 28 days for each blend. However, this trend disappears from 28-day to 56-day and there is a considerable increase in the 56-day strengths compared to the 28-day strengths. This increase was particularly prominent for the 10Mg mix (Fig. 5).

3.3.2 Effect of carbonation on compressive strength

All mixes presented strength loss after the carbonation process, except 5Mg10Mk and cement-based mixes. The greatest decrease of 65% was observed in the 100S mix. It is a well-known phenomenon that the main reason for this decline is the decalcification of C-(A)-S-H gel. Carbonation of pore solution reduces its alkalinity and this causes decalcification of the C-(A)-S-H phase, leading to the degradation of the chain structure and the consequent formation of an aluminosilicate type gel product [39]. Bernal et al. [66] stated that the compressive strength of sodium silicate activated-slag decreased by approximately 60% after 540 h of CO_2 exposure. They also stated that under lower M_s ratios (SiO_2/Na_2O ratio), samples are susceptible to carbonation at a higher amount in metakaolin-free samples; however, in case of metakaolin is added into the system, this trend is reversed due to the formation of secondary aluminosilicate phases. Similarly, in this study, Mg and Mk incorporation reduced the strength loss on NC-activated slag-based mixes compared to the 100S. Strength losses were 24% and 37% for 10Mg and 10Mg5Mk mixes, respectively. One of the reasons for lower strength loss is due to the presence of Al ions from Mk and Mg ions from MgO that leads to the formation of hydrotalcite, which is resistant and stable under the carbonation effect.

The strength loss for the control mix 100S and also for Mg- and Mk-substituted mixes were approved with the microstructural analysis of XRD and SEM (Figs. 7-8 and 17-18). An increase in the strength of 5Mg10Mk mixes was observed after the accelerated carbonation effect and reached two times higher strength values (2.5 MPa). Even the strength value increased to two

times higher values; however, it was still relatively low to be used as a structural material. The strength increment was attributed to the additional calcite formation, which was displayed in the XRD, TG, and SEM analysis (Figs. 8 and 18). Moreover, the cement-based mix represented an increase in the compressive strength after the carbonation effect. It was attributed to the deposition of the carbonation reaction products, which cause pore size refinement [69].

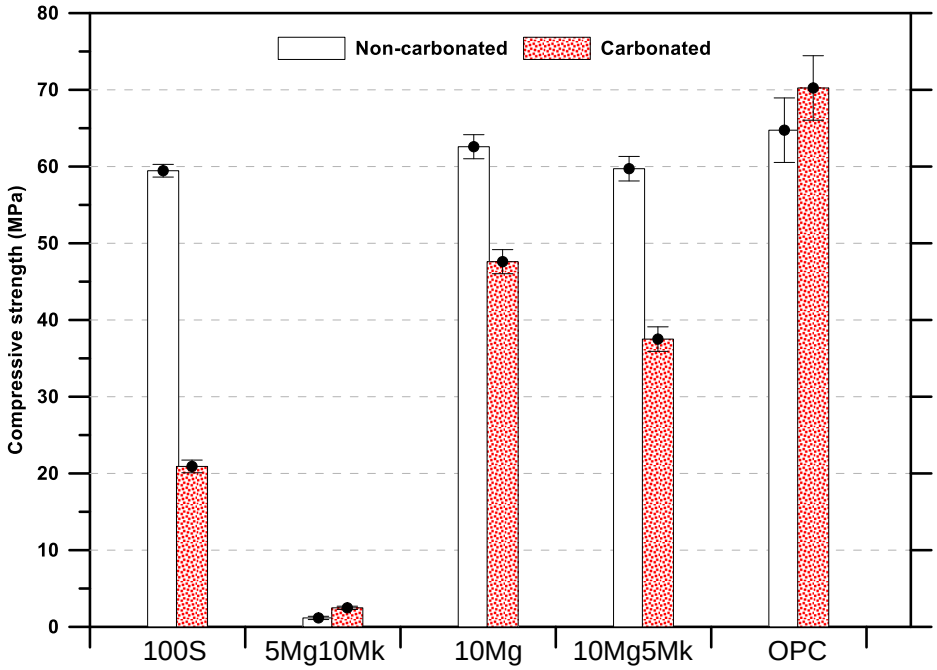

Fig. 6. Compressive strength values of non-carbonated and carbonated mixes at 56 days.

3.4 X-ray diffraction analysis

Fig. 7 shows XRD patterns of non-carbonated NC-activated mixes. Unlike the XRD pattern of raw slag (Fig. 2), which shows a broad hump at around 25-35° 2θ, prominent peaks were observed in all alkaline activated mixes. The formation of tobermorite like C-(A)-S-H phase was identified at around 29° 2θ, which is sharper and more pronounced in the 100S, 10 Mg, and 10Mg5Mk mixes when compared to the 5Mg10Mk mix with a broader hump between 25° 2θ and 35° 2θ suggesting an amorphous binder structure. Furthermore, hydrotalcite-like phase ($Mg_6Al_2(CO_3)(OH)_{16}\cdot 4(H_2O)$) has also been identified in all mixes at 22.9° 2θ and 39.4° 2θ angles. Periclase (MgO) is identified, which diffracts at 37° 2θ and 62.3° 2θ in mixes with Mg substitution (i.e., 5Mg10M, 10Mg and 10Mg5Mk). Moreover, a minor quartz peak is observed at 26.7° 2θ in the 5Mg10Mk and 10Mg mixes. In addition, zeolite is found around 12° 2θ diffraction angle with a broader hump in the 10Mg and 10Mg5Mk mixes.

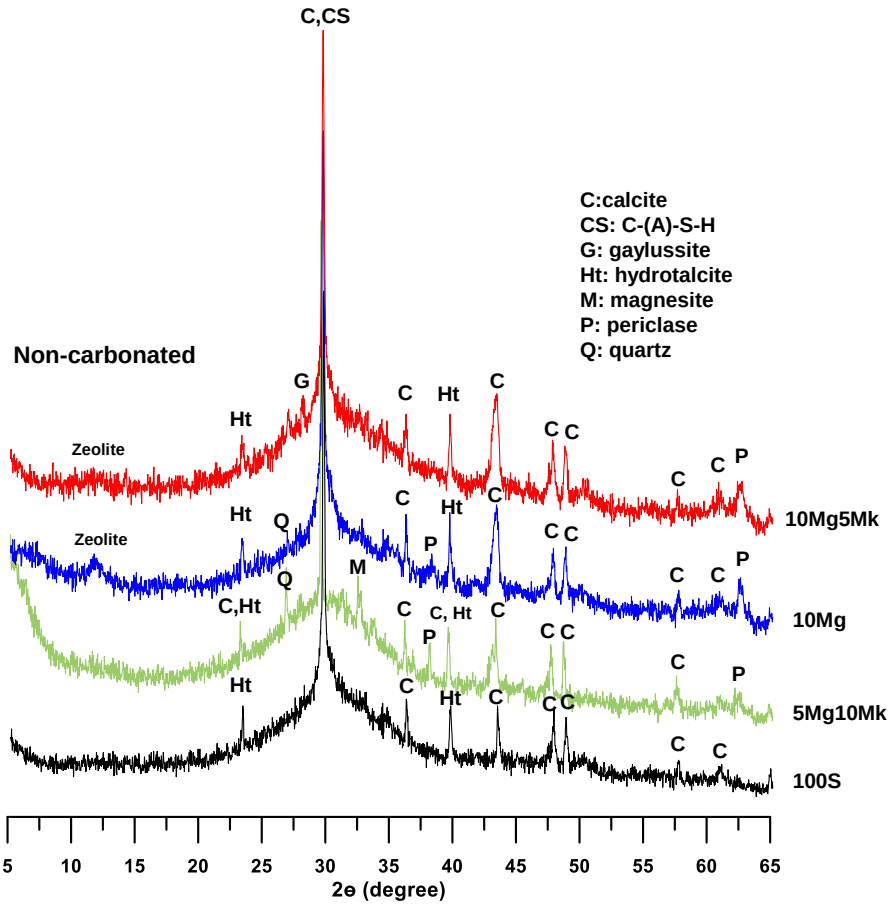

Fig. 7. XRD patterns of non-carbonated mixes at 56 days.

Fig. 8 shows XRD patterns of carbonated NC-activated mixes. The general trend shows that the sharp calcite, hydrotalcite, and C-(A)-S-H peaks in the mixes become broader after the accelerated carbonation. This is attributed to decalcification which leads to strength loss of carbonated 100S, 10Mg, and 10Mg5Mk specimens. For the carbonated 100S sample, quartz peak diffracts at about 31° 2θ is formed, indicating decalcification of C-(A)-S-H gel. For the 10Mg sample, dolomite ($CaMg(CO_3)_2$) is identified at several diffraction angles, 31° 2θ in particular. Thus, strength loss of the 10Mg mix may be attributed to the decomposition and conversion of C-(A)-S-H into dolomite. Furthermore, diopside ($CaMgSi_2O_6$) is also formed, which does not contribute to the strength of the carbonated specimens. The zeolite peak in the carbonated sample is more distinct compared to the non-carbonated sample. Moreover, hydrotalcite and C-(A)-S-H peaks are broader in the 10Mg mix. Similar to the 10Mg mix, diopside is also observed in the 10Mg5Mk mix. The hydrotalcite and calcite peaks remain sharp in the 10Mg5Mk mix. However, the C-(A)-S-H peak is also broader than the non-carbonated case, resulting from decalcification. For the 5Mg10Mk mixes, quartz is formed after accelerated carbonation. Similar to the non-carbonated 5Mg10Mk sample, a broad C-(A)-S-H gel peak is observed in the carbonated 5Mg10Mk sample.

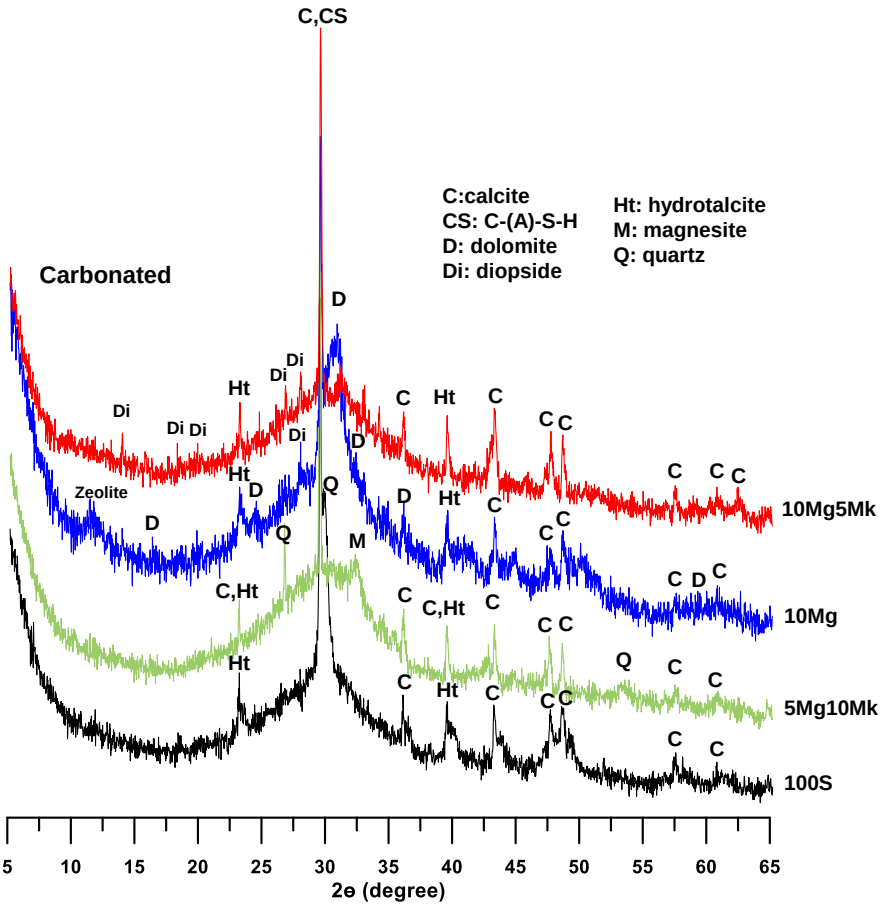

Fig. 8. XRD patterns of carbonated mixes at 56 days.

3.5 FTIR analysis

Fig. 9 shows FTIR patterns of non-carbonated NC-activated mixes. The bonds located around 870 cm^{-1} and 1412 cm^{-1} were observed due to the stretching vibration of O-C-O bonds of carbonate groups υ_3-CO_3^{2-} and υ_2-CO_3^{2-}, respectively [70–72], which suggest the formation of carbonate-containing phases such as calcite, dolomite, and magnesite. The shoulder at 870 cm^{-1} also accounts for the asymmetric stretch of AlO_4^- groups [70,71]. The broad and weak band at around 713 cm^{-1} is related to the bending of Al–O–Si bonds [73,74], due to C-(A)-S-H gel formation.

Bending vibration of H-O-H bonds at about 1645-1650 cm^{-1} is found, which is attributed to chemically bound water [70,71,75]. The wavenumber of this bond did not change either with the Mg and Mk substitution or carbonation effect. The main peak at 956 cm^{-1} is attributed to the formation of C-(A)-S-H, which is asymmetric stretching vibration of Si–O–T bonds generated by Q^2 units, where T is referred to silicon or aluminium [71,75,76]. It can be seen that for all mixes, the Si–O–T band was around 956 cm^{-1}, while for the 5Mg10Mk mix this value was higher (964 cm^{-1}). This relatively higher wavenumber is due to the lower Ca/Si ratio formed in 5Mg10Mk mixes. This reveals that the substitution of a high amount of M increases the polymerization degree of Si-O in C-(A)-S-H by providing more silicate [77]. Bernal et al. [66] stated that incorporation of 10% of Mk into the alkali silicate-activated slag led to a shift in the asymmetric stretching vibration of the Si–O–T bonds to higher wavenumbers, suggesting that the samples are more highly polymerize as a consequence of the higher Al content leading to condensation of tetrahedral species [70,78]. For other NC-activated mixes, no considerable

shift of wavenumber was found with the substitution of Mg or Mk. In addition, higher intensities for this band were observed for all NC-activated mixes except 5Mg10Mk. The higher intensity shows a high quantity of formation of reaction products, contributing positively to the higher mechanical strength (Fig. 5).

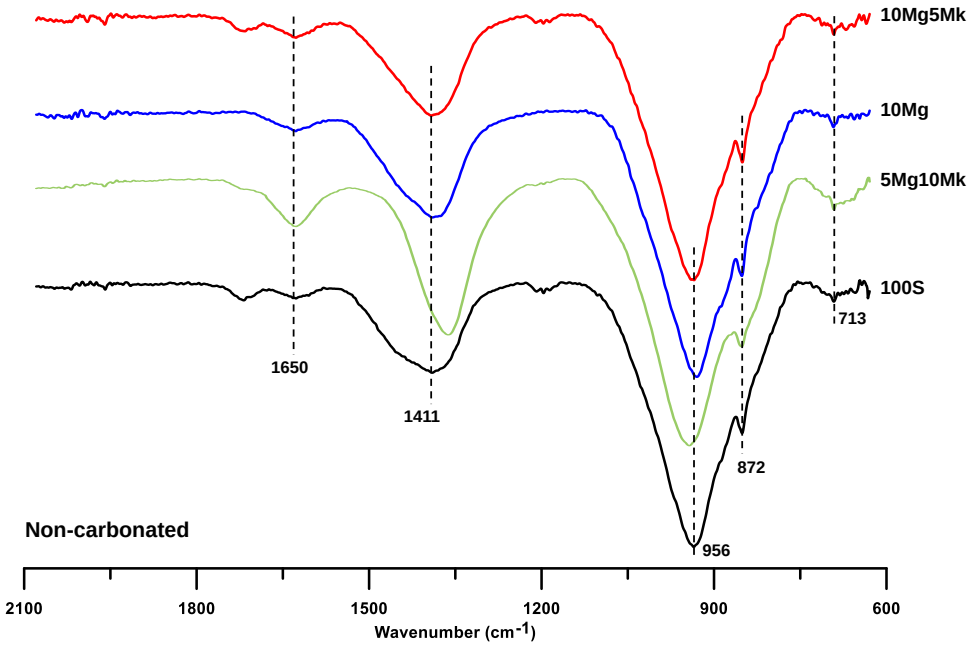

Figure. FTIR spectra of non-carbonated mixes at 56 days

Fig. 9. FTIR spectra of non-carbonated mixes at 56 days.

Fig. 10 shows FTIR patterns of carbonated NC-activated mixes, revealing similar vibration modes. The Si–O peak in all samples shift to the higher wavenumber, from 956 cm^{-1} to 992 cm^{-1}, demonstrating a higher degree of polymerization of silicates and the formation of a silicate with a very low concentration of calcium [79–81]. This indicates decalcification of the C-(A)-S-H phase followed by the formation of amorphous silica gel as identified at 784 cm^{-1} [82,83], which their intensities of characteristic bands increase for carbonated mixes. Higher intensities for bending vibration at 874 cm^{-1} and stretching vibration at 1412 cm^{-1} of O–C–O bonds found in the carbonated groups associated with the formation of higher calcium carbonate.

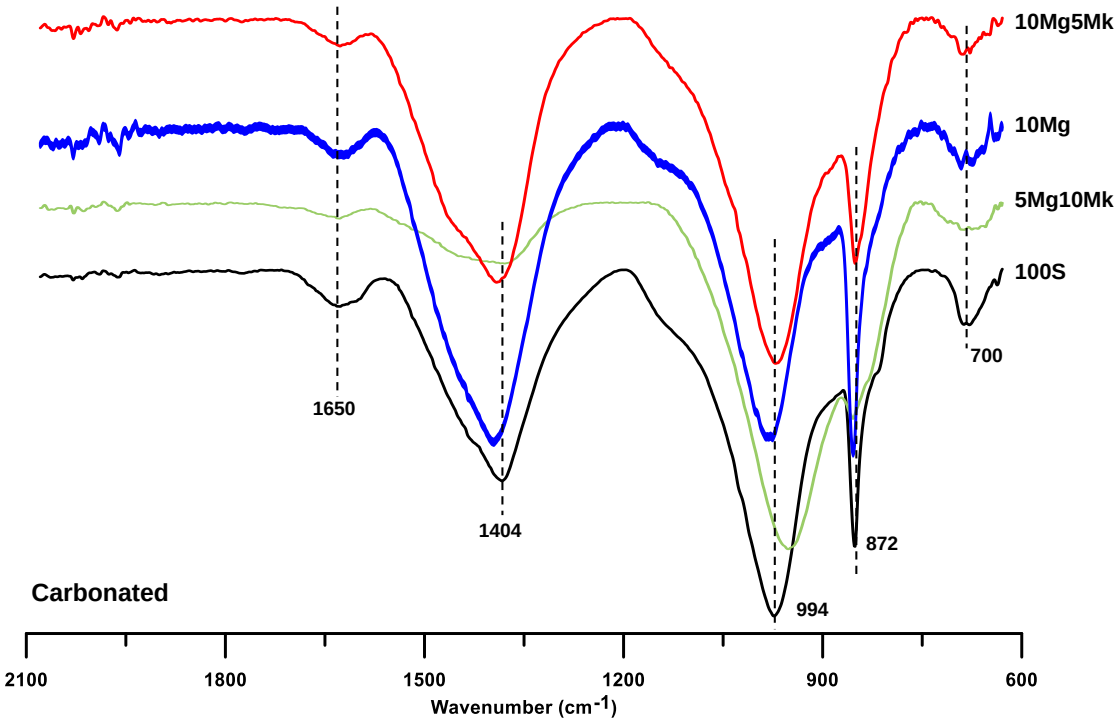

Fig. 10. FTIR spectra of carbonated mixes at 56 days.

3.6 Thermogravimetric analysis of reaction products

Thermogravimetric tests were performed to examine the phase transition of non-carbonated and carbonated groups at 56 days for each mix and the test results are given in Figs. 11-14. Several typical decomposition peaks were detected for all mixes. The first and major mass loss between 50°C and 250°C is associated with evaporation of the free water and/or bound water from the C-(A)-S-H phase [84,85]. A hump peak positioned at about 120°C is related with the dehydration of the C-(A)-S-H gel [86]. For 5Mg10Mk, the low peak temperature indicates a weak phase. Higher mass losses were observed with the Mg and Mk substitution for both non-carbonated and carbonated samples. The higher water content is related to C-(A)-S-H phase may be associated with high alkali activation of the binders or adsorption of more water in the C-(A)-S-H phase due to the presence of a higher amount of alkalis in the interlayer of the C-(A)-S-H phase [87]. The second peak from 250°C to 450°C is due to the dehydroxylation of hydrotalcite [88,89], conforms to the XRD results (Fig. 7). The third small broad peak, around 700°C, is formed by the decomposition of carbonates such as calcite [90] and gaylussite. The mass losses of samples incorporating Mg and Mk were higher than that of the control mix 100S, complying with the compressive strength results.

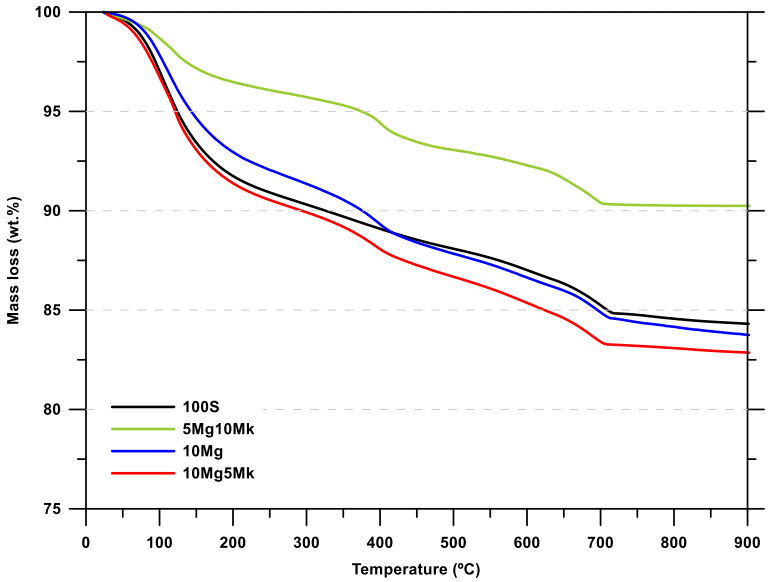

Fig. 11. TG curves of non-carbonated mixes at 56 days.

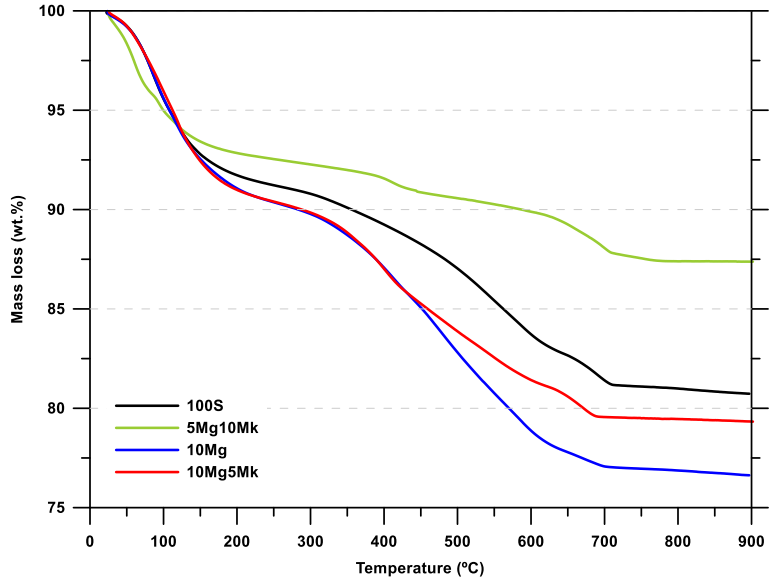

Fig. 12. TG curves of carbonated mixes at 56 days.

DTG curves changed significantly for carbonated mixes. Firstly, the peaks related to C-(A)-S-H decomposition decreased in all carbonated mixes. The reduced intensity of the first peak is associated with the decalcification of C-(A)-S-H (and/or silica gel formation). Only 5Mg10Mk presented an increase consistent with the strength increase. 10Mg mixes exhibited a minor change, which indicates that the substitution of Mg results in more residual molecular water in C-(A)-S-H gel for carbonated mixes. This also may explain the highest strength for 10Mg mixes among the other carbonated mixes (Fig. 6). The increased intensity of the peak around 700°C is associated with the decomposition of a higher amount of carbonate-containing phases. 5Mg10Mk presented a considerable increase in the intensity for this peak, which is consistent with the SEM results (Fig. 19). Decomposition of carbonate-containing phases has started at the earliest for 5Mg10Mk mixes compared to others.

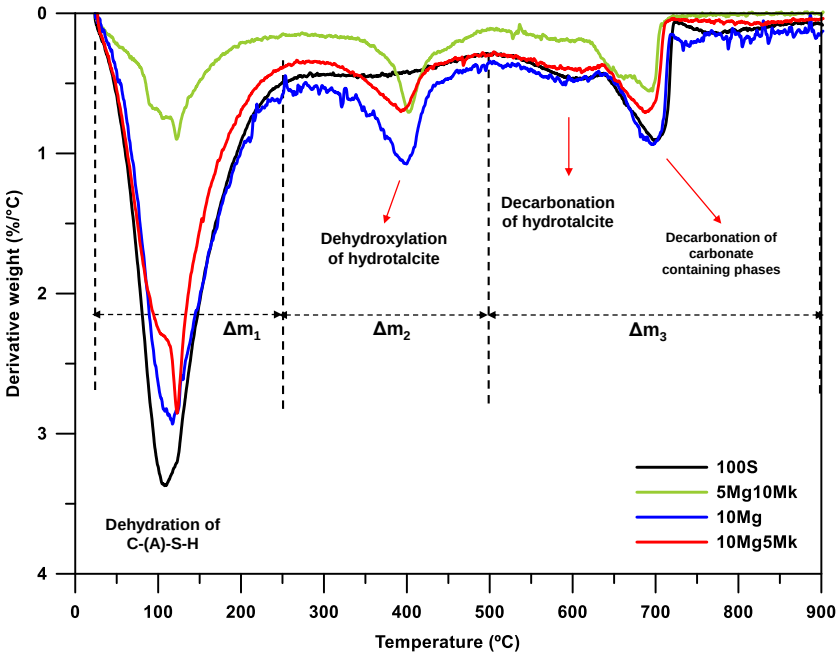

Fig. 13. DTG curves of non-carbonated mixes at 56 days.

For carbonated situation, the 10Mg mix formed a broad DTG peak between 250°C and 600°C associated with the mass losses of dehydroxylation of hydrotalcite, decarbonation of poorly crystalline calcite and decarbonation of hydrotalcite. The distinct peak appearing at around 700°C is associated with calcite and other carbonate-containing phases such as dolomite and magnesite, which is approved in the XRD patterns (Fig. 8). The broad DTG peak related to the decomposition of carbonate-containing phases at a relatively lower temperature range suggests the amorphous form of carbonate-containing phases. These amorphous phases tend to form in the samples incorporating metakaolin as the decomposition temperature of carbonate-containing phases is relatively lower for 5Mg10Mk and 10Mg5Mk mixes. This conclusion agrees with the XRD analysis results (Fig. 8) since carbonate containing phases such as calcite, magnesite and dolomite shows amorphous peaks.

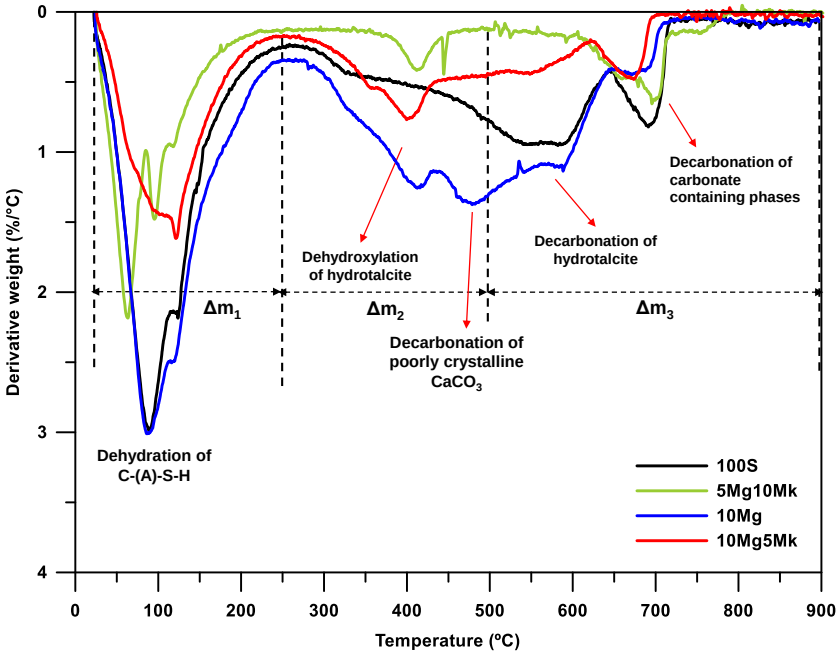

Fig. 14. DTG curves of carbonated mixes at 56 days.

The weight loss was divided into three groups based on the temperature ranges of 25°C-250°C (Δm_1), 250°C-500°C (Δm_2), 500°C-900°C (Δm_3) (Table 3). The first temperature interval is associated with the dehydration of the reaction products such as C-(A)-S-H. The second one is due to dehydroxylation of hydrotalcite and decomposition of hydrotalcite, and the third one designates decarbonation of carbonate-containing phases. The maximum mass loss was obtained in the first range, between 25°C -250°C (Δm_1) for all mixes and both cases. The mass loss of C-(A)-S-H was 9% for 100S and 7.9% and 9.5% for 10Mg and 10Mg5Mk mixes, respectively (Table 3). 5Mg10Mk had the lowest value as 3.9%. The value of Δm_1 increased with the Mg and Mk substitution, which indicates a higher degree of reaction.

The mass loss between 250°C and 500°C (Δm_2) increased with the Mg and Mk substitution (Table 3). 5Mg10Mk mixes presented the lowest value among the carbonated mixes. On the other hand, except 5Mg10Mk, Δm_3 was similar for all mixes ranged between 3.8% and 4.1% for non-carbonated mixes. The Δm_1 value decreased or remained similar for 100S and 10Mg5Mk carbonated mixes, while a considerable increase was seen on 5Mg10Mk. The obtained increase in 5Mg10Mk was from 3.9% to 7.4% due to the carbonation. An increase in Δm_2 and Δm_3 shows a greater formation of carbonate-containing phases in all mixes (Table 3).

Table 3. Mass loss values of non-carbonated and carbonated mixes

Mixes	Mass loss (wt. %)							
	Non-carbonated mixes				Carbonated mixes			
	Δm_1	Δm_2	Δm_3	Total	Δm_1	Δm_2	Δm_3	Total
100S	9.0	2.8	3.8	15.7	8.6	4.2	6.3	19.2
5Mg10Mk	3.9	3.0	2.8	9.7	7.4	2.0	3.2	12.6
10Mg	7.9	4.2	4.1	16.3	9.5	7.6	6.2	23.9
10Mg5Mk	9.5	3.9	3.8	17.1	9.6	6.5	4.6	20.7

3.7 Solid-state NMR

Solid-state NMR was utilised to further investigate the chemical structure of the NC-activated mixes. Fig. 15 shows the ^{27}Al MAS NMR spectra of the non-carbonated and carbonated mixes after 56 days of curing, alongside the precursor mixes of 100S and 5Mg10Mk for comparison. As demonstrated in the spectra of the precursors, slag consists of Al in an amorphous AlO_4 environment (80-50 ppm) [13,91–94] while metakaolin contains amorphous AlO_4, AlO_5 (50-30 ppm) and AlO_6 (15-0 ppm) environments [42,95]. Upon curing, all mixes show narrowing of the AlO_4 resonance and the appearance of a crystalline AlO_6 resonance at 11 ppm, suggesting that the majority of the Al in the mixes is involved in the reaction. The crystalline AlO_6 resonance can be assigned to the formation of hydrotalcite [13,94,96]. The AlO_4:AlO_6 ratio for each mix can be seen in Table 4, which shows that 10 Mg has the highest hydrotalcite formation corroborating its highest compressive strength. Mixes 10Mg5Mk and 100S also demonstrate hydrotalcite formation, whereas the AlO_6 ratio of 5Mg10Mk does not increase from its precursor value suggesting that negligible hydrotalcite formation occurs. The AlO_4 resonance of 5Mg10Mk also appears different from the other mixes with a centre of gravity of 62 ppm, compared to 65-66 ppm. This shift to higher frequencies is likely due to the influence of Ca in the C-(A)-S-H gel formed in 100S, 10Mg, and 10Mg5Mk, while the finer structure evident in the line shapes of the AlO_4 resonances suggests a crystalline environment [92,94,96].
Upon carbonation, the ^{27}Al spectra can be seen to change for 100S, 10Mg and 10Mg5Mk, whereas 5Mg10Mk remains mostly unchanged. The AlO_6 ratios fall in the former samples

corroborating the loss of hydrotalcite seen in the XRD results. In addition, the AlO_4 resonances shift to 59-62 ppm for all samples, confirming the decalcification of the C-(A)-S-H gel upon carbonation.

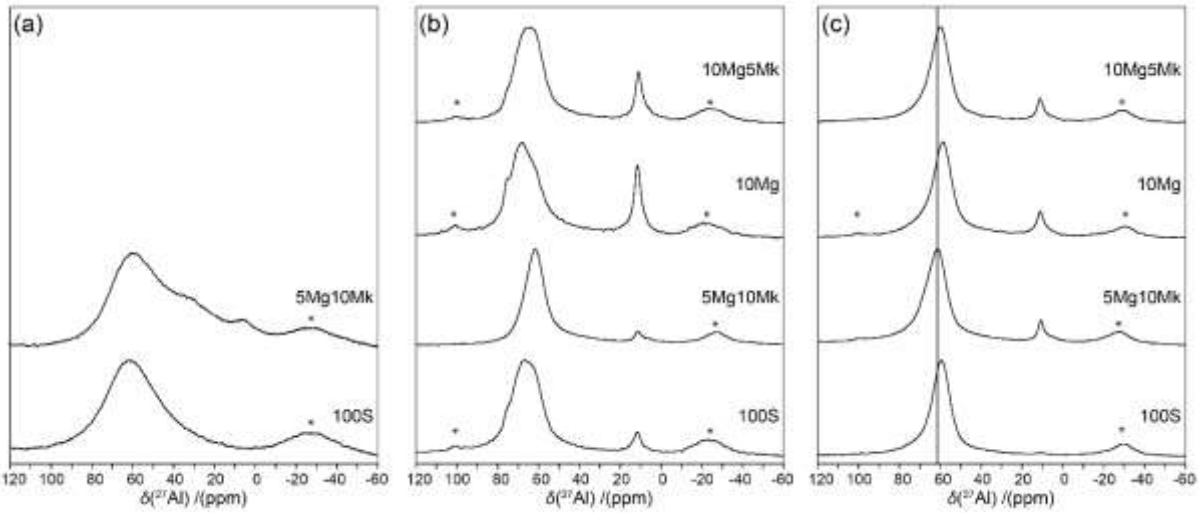

Fig. 15. The ^{27}Al MAS NMR spectra of powdered (a) precursor, (b) non-carbonated and (c) carbonated mixes. Asterisks mark MAS sidebands.

Table 4. Relative integrals of the ^{27}Al NMR resonances of the mixes.

Treatment	Mixes	Relative integral (%)	
		AlO_4	AlO_6
Precursors	100S	100	0
	5Mg10Mk	88	12
Non-carbonated	100S	91	9
	5Mg10Mk	91	9
	10Mg	79	21
	10Mg5Mk	83	17
Carbonated	100S	97	3
	5Mg10Mk	90	11
	10Mg	87	13
	10Mg5Mk	88	12

Fig. 16 shows the ^{29}Si MAS NMR spectra of the non-carbonated and carbonated mixes after 56 days of curing, alongside the spectra of the precursor mixes of 100S and 5Mg10Mk for comparison. The differing connectivity of Si(IV) moieties in aluminosilicate compounds results in characteristic ^{29}Si NMR chemical shifts between -60 and -120 ppm. These distinct moieties are commonly labelled as $Q^n(mAl)$, where n is the number of O mediated bonds to adjacent SiO_4/AlO_4 units and m is the amount of Al units involved. As demonstrated by the spectra of the 100S precursor, slag contains two broad resonances at -79 and -111 ppm, corresponding to amorphous Q^1 moieties and amorphous Q^4 moieties, respectively, with the latter corresponding to the presence of amorphous silica (SiO_2) [13] [91,92,94,97]. The spectra of the 5Mg10Mk precursor demonstrates the introduction of Mk with a third broad resonance around -105 ppm [42,95]. Table 5, 6 and 7 detail the relative integrals of the ^{29}Si resonances and their assignments.

The spectra of the non-carbonated mixes (Fig. 16 (b)) demonstrate the changes to the Si environments during curing. Narrow resonances have appeared in mixes 100S, 10Mg and 10Mg5Mk at -79, -82 and -85 ppm. These resonances are well known, and correspond to crystalline Q^1(0Al), Q^2(1Al) and Q^2(0Al) moieties which make up the C-(A)-S-H structure [13,18,91,92,94]. 10Mg can be seen to have the highest crystalline C-(A)-S-H content, corroborating its high compressive strength, whereas 5Mg10Mk forms none. A broader resonance around -86 ppm can be seen in each of the spectra, which can be assigned as amorphous Q^2 product. The fits did not require a resonance at -105 ppm, which would have been assigned as remaining Mk. The lack of any Mk remaining in 5Mg10Mk is likely unrealistic due to the supposed increase in the silica Q^4 environment, which should not be involved in the reaction. Instead, the Mk environment is likely to make up part of the overlapping shoulders of the broad resonances at -86 and -111 ppm.

Upon carbonation (see Fig. 16 (c)), the crystalline C-(A)-S-H resonances are all lost, confirming the degradation of the C-(A)-S-H gel. A broad resonance around -98 ppm replaces these resonances, which is assigned as amorphous Q^4 moieties in a highly-linked aluminosilicate network (ASN) [42,98]. A small narrow resonance at -93 ppm can be observed in mixes 100S, 10Mg and 10Mg5Mk, which has previously been assigned as a small amount of crystalline Q^4(3Al) in the ASN formed via decalcification [38,42,98]. 5Mg10Mk remains unchanged, much like the ^{27}Al data, due to the lack of crystalline C-(A)-S-H prior to carbonation.

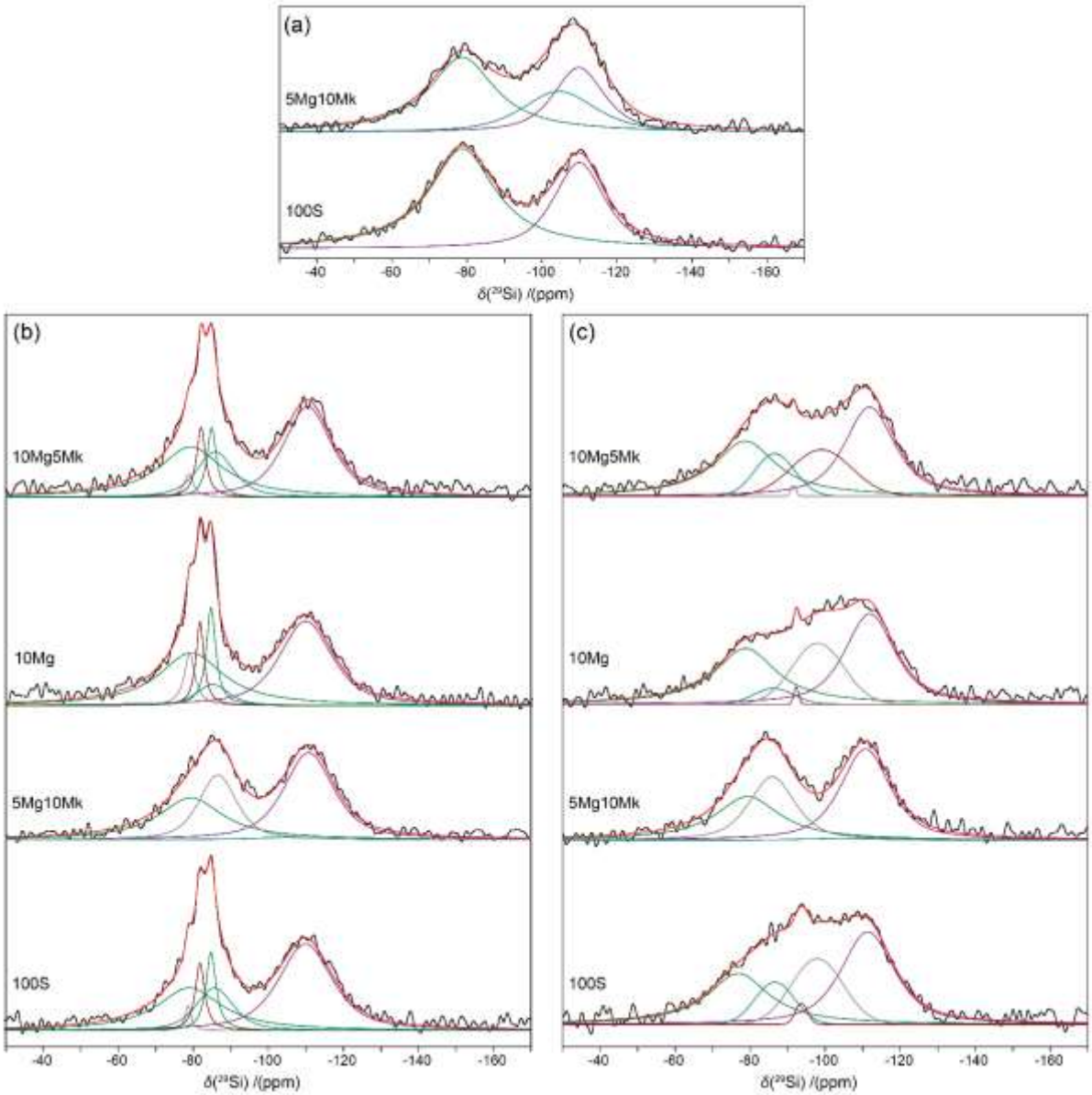

Fig. 16. The ^{29}Si MAS NMR spectra of powdered (a) precursor, (b) non-carbonated and (c) carbonated mixes. Experimental spectra, simulated line shapes and deconvoluted resonances are in black, red and multi-coloured respectively. Asterisks mark MAS sidebands.

Table 5. Relative integrals of the ^{29}Si NMR resonances of the precursor mixes, with environment assignments and mean chemical shifts.

Mixes	Relative integrals (%)		
	slag Q^1	silica Q^4	Mk
	-78.9 ppm	*-110.8 ppm*	*-104.8 ppm*
pre 100S	63	37	
pre 5Mg10Mk	47	28	25

Table 6. Relative integrals of the ^{29}Si NMR resonances of the non-carbonated mixes, with environment assignments and mean chemical shifts.

Mixes	Relative integrals (%)					
	slag Q^1 *-78.9 ppm*	silica Q^4 *-110.8 ppm*	amorph. Q^2 *-86.1 ppm*	C-(A)-S-H Q^1(0Al) *-78.9 ppm*	C-(A)-S-H Q^2(1Al) *-82.0 ppm*	C-(A)-S-H Q^2(0Al) *-84.9 ppm*
100S	27	42	14	2	7	8
5Mg10Mk	30	44	26			
10Mg	33	39	6	6	7	9
10Mg5Mk	31	38	15	2	7	7

Table 7. Relative integrals of the ^{29}Si NMR resonances of the carbonated mixes, with environment assignments and mean chemical shifts.

Mixes	Relative integrals (%)				
	slag Q^1 *-78.9 ppm*	silica Q^4 *-110.8 ppm*	amorph. Q^2 *-86.1 ppm*	amorph. ASN *-98.4 ppm*	ASN Q^4(3Al) *-92.6 ppm*
100S	27	39	11	22	1
5Mg10Mk	29	43	28		
10Mg	34	39	4	22	1
10Mg5Mk	31	38	11	19	1

3.8 Microstructural characterization by SEM-EDS

The morphologies of non-carbonated and carbonated paste samples at 56 days were determined using SEM. The microstructure images of non-carbonated samples are shown in Fig. 17 ((a)-(d)), while carbonated samples are shown in Fig. 17 ((a)-(d)). In the control mix, 100S, the formation of a solid and dense matrix was visible, without loosely packed particles. 10Mg and 10Mg5Mk mixes also showed a homogeneous and dense structure. However, 5Mg10Mk showed a high amount of unreacted slag particles and a loose structure compared with other mixes, consistent with low compressive strength and less extent of reaction.

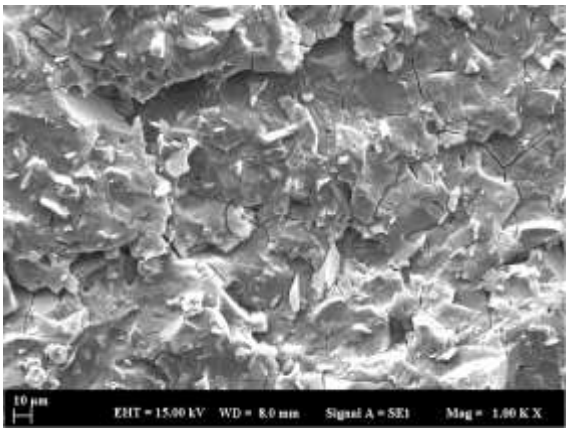

(a)

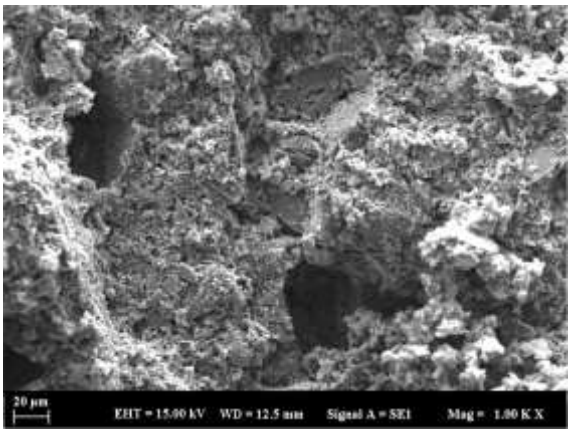

(b)

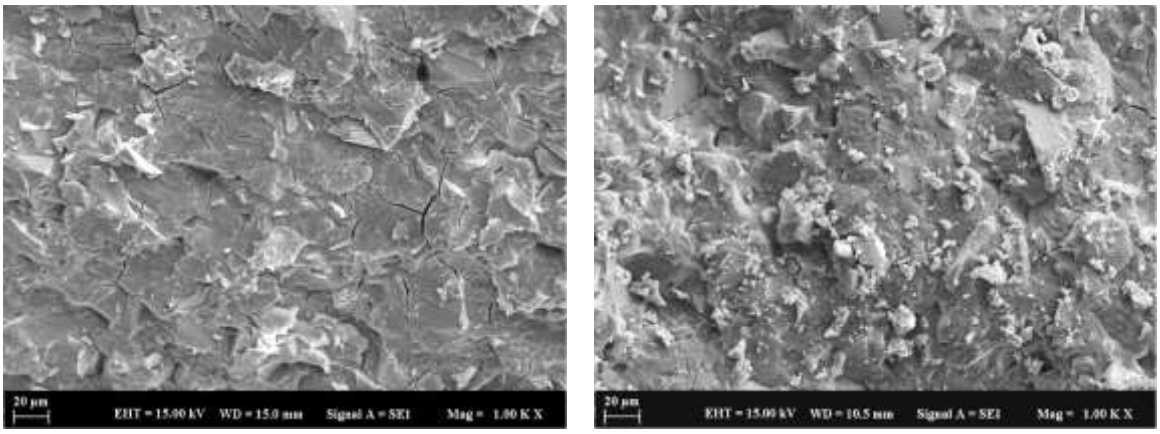

(c) (d)

Fig. 17. Secondary electron images of non-carbonated mixes at 56 days at 1,000× magnification (a) 100S, (b) 5Mg10Mk, (c) 10Mg and (d) 10Mg5Mk.

Relatively porous structure was observed for 100S mixes and calcite formation on the surface of the paste samples were identified (Fig. 18 (a)) under the carbonation effect. This relatively loose structure of 100S could be caused by the decalcification of the C-(A)-S-H gel, which is a reason for strength reduction observed in compressive strength for carbonated mixes. On 5Mg10Mk mixes (Fig. 18 (b)), a higher amount of calcite was seen due to the carbonation effect, which was also observed in XRD and TG analysis. It was assumed that this additionally formed calcite may be slightly contributed to the compressive strength of 5Mg10Mk, which reached higher values compared to non-carbonated situation.

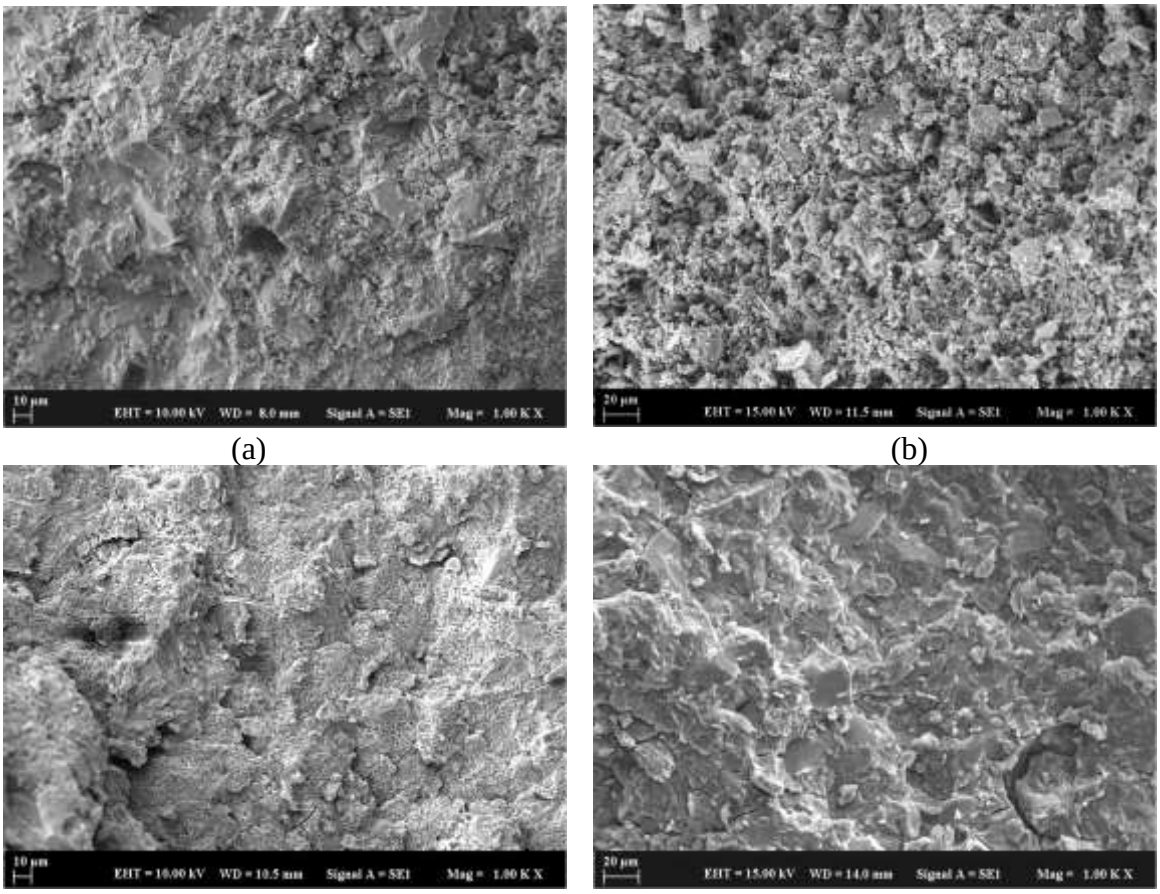

(a) (b)

(c) (d)

Fig. 18. Secondary electron images of carbonated mixes at 56 days at 1,000× magnification (a) 100S, (b) 5Mg10Mk, (c) 10Mg and (d) 10Mg5Mk.

It can be seen that under high magnifications, e.g., 10,000 ×, micro-cracks were observed in 100S (Fig. 19 (a)), which is consistent with the lower compressive strength of carbonated mixes. On the other hand, new phases are identified, wrapping the C-(A)-S-H gel or unhydrated slag particles in Mg-substituted mixes, 10Mg and 10Mg5Mk (Fig. 19 (b) and (c)). According to the SEM-EDS point analysis (Fig. 20), this new phase is Na, Si, Ca-enriched and contains Mg^{2+} and Al^{3+} ions. For 5Mg10Mk, a porous structure and calcite formation can be seen more easily from Fig. 19 (d).

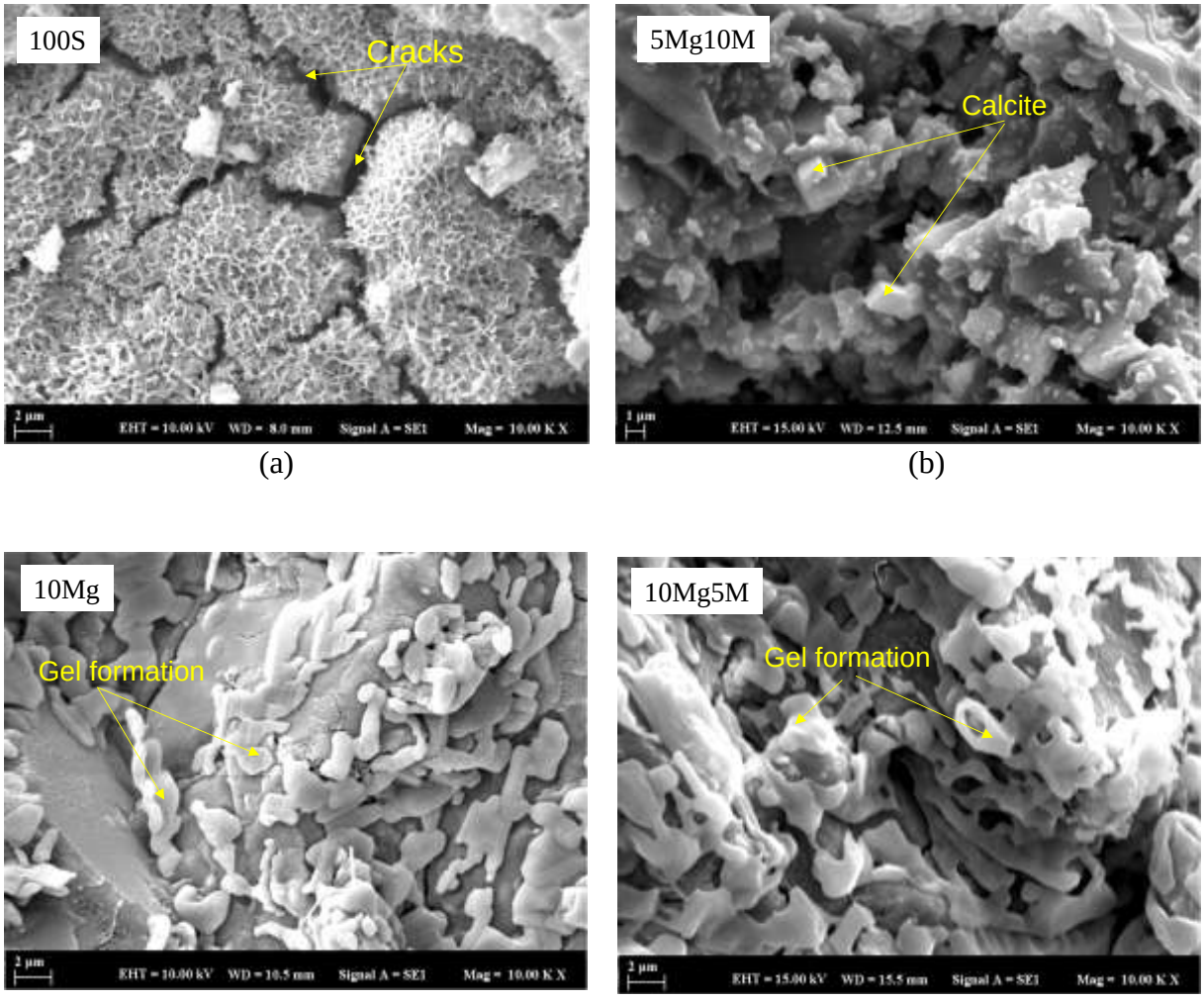

(a) (b)

(b) (d)

Fig. 19. Secondary electron images of carbonated mixes at 56 days at 10,000× magnification (a) 100S, (b) 10Mg, (c) 10Mg5Mk and (d) 5Mg10Mk.

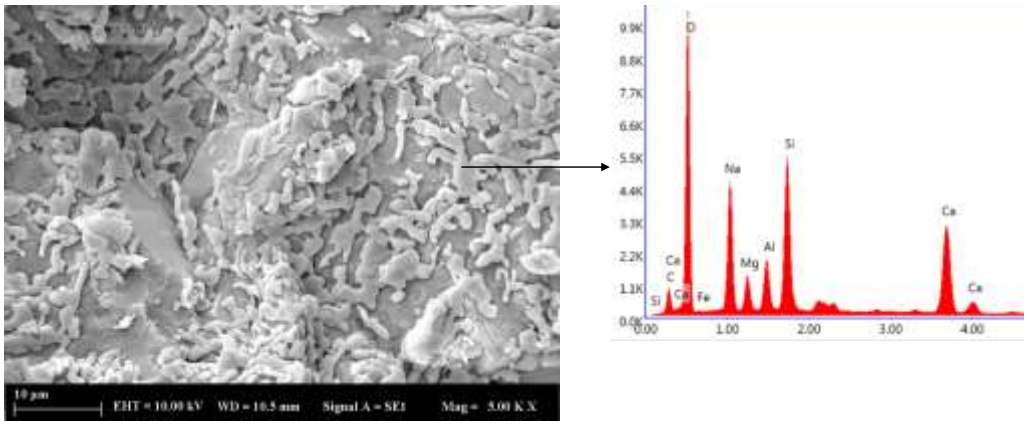

Fig. 20. Secondary electron image of carbonated 10Mg5Mk, showing gel formation under carbonation.

BSE images of the mixes at 1,000× magnification reveals the effects of Mg and Mk-substitution on the microstructure of the NC-activated slag-based mixes after 56 days of curing (Fig. 21 ((a)-(d)). The dark grey tone recognizes in the images attributed to the unreacted slag particles, while the lighter grey part surrounding the particles shows one of the main hydration products; C-(A)-S-H or C-(N,A)-S-H. Also, carbonate-containing products such as calcite was observed with white colour. It can be seen from these images that while 5Mg10Mk mixes presented a very high amount of unreacted slag or metakaolin particles and very low binder phases, the other mixes, especially Mg- and Mk-substituted 10Mg5Mk mixes, presented very low amount and smaller size of unreacted precursor particles. The smaller size of unhydrated precursor particles in 10Mg5Mk demonstrates a denser and strong matrix, indicating the contribution of Mg and Mk to the hydration and thus improving the performance of NC-activated slag-based systems.

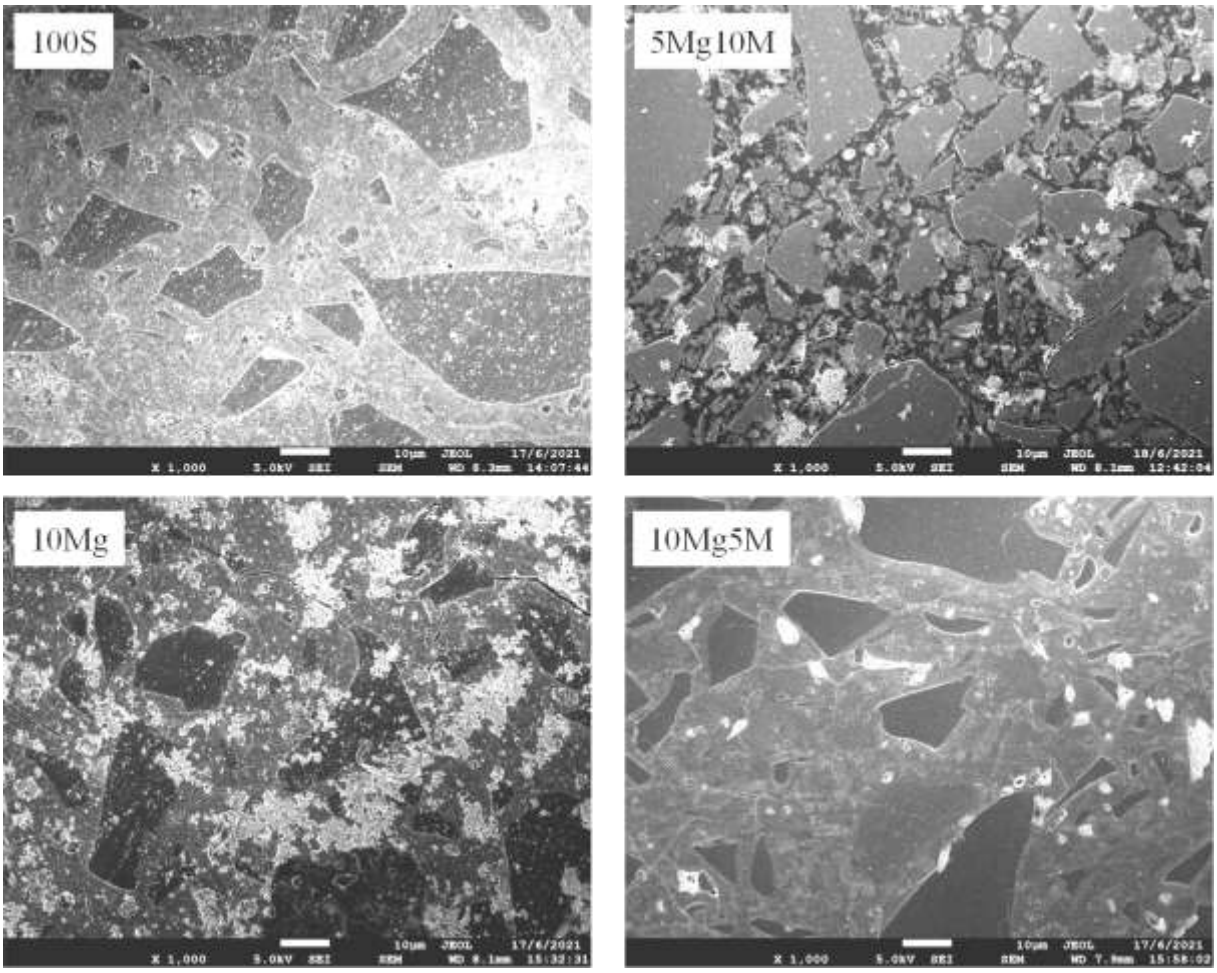

Fig. 21. Backscattered electron images of mixes at 1,000× magnification.

The EDS results show that the hydration products primarily consist of Na, Al, Ca, Si, Mg, and O elements. It can be figured out that the main gel product of the mixes is C-(N,A)-S-H gel, since a large number of Na, Si, Al, Ca elements are seen (Figure 22, point 3 and Fig. 23, point 2). The atomic ratios of Ca/Si are 0.64 and 0.54 for 10Mg and 10Mg5Mk mixes, while Si/Al ratios are 3.00 and 2.49, respectively. On the other hand, the atomic ratio of Na/Al is about 1.55, and the atomic ratios of Si/Al are 2.49 and 3.00, which conforms to the theoretical molar ratio of Na/Al ≈ 1 and Si/Al ≈ 1–3 [99]. On the other hand, unhydrated slag particles (Fig. 22, point 2 and Fig. 23, point 1) and calcite formation (Fig. 22, point 1) are also determined.

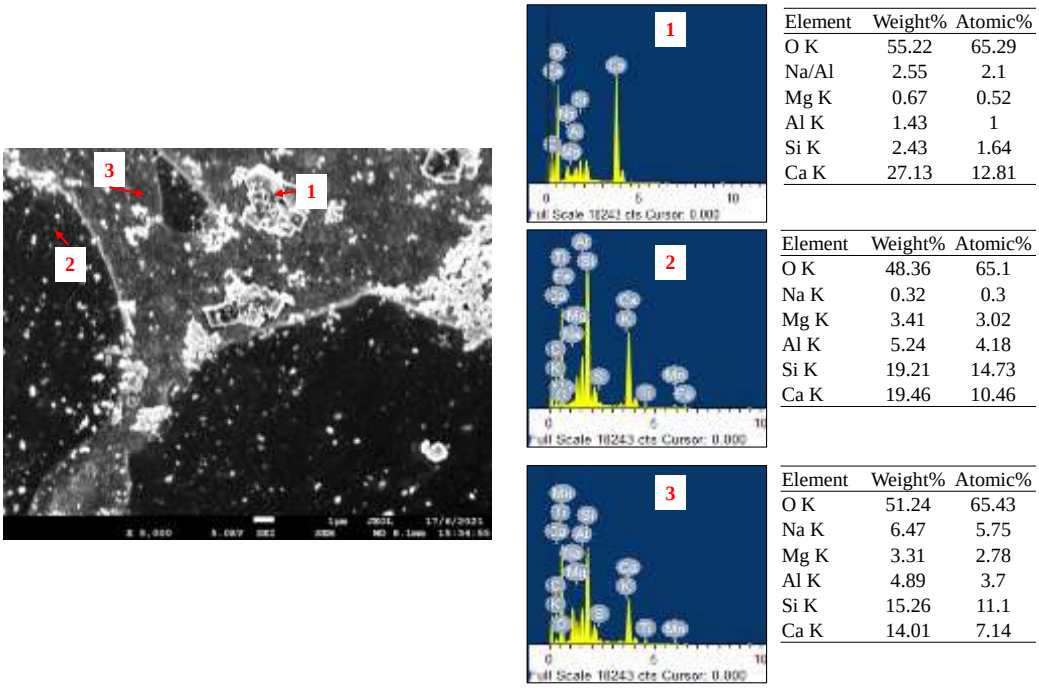

Element	Weight%	Atomic%
O K	55.22	65.29
Na/Al	2.55	2.1
Mg K	0.67	0.52
Al K	1.43	1
Si K	2.43	1.64
Ca K	27.13	12.81

Element	Weight%	Atomic%
O K	48.36	65.1
Na K	0.32	0.3
Mg K	3.41	3.02
Al K	5.24	4.18
Si K	19.21	14.73
Ca K	19.46	10.46

Element	Weight%	Atomic%
O K	51.24	65.43
Na K	6.47	5.75
Mg K	3.31	2.78
Al K	4.89	3.7
Si K	15.26	11.1
Ca K	14.01	7.14

Fig. 22. EDS spectrum and elemental analysis at different points of 10Mg.

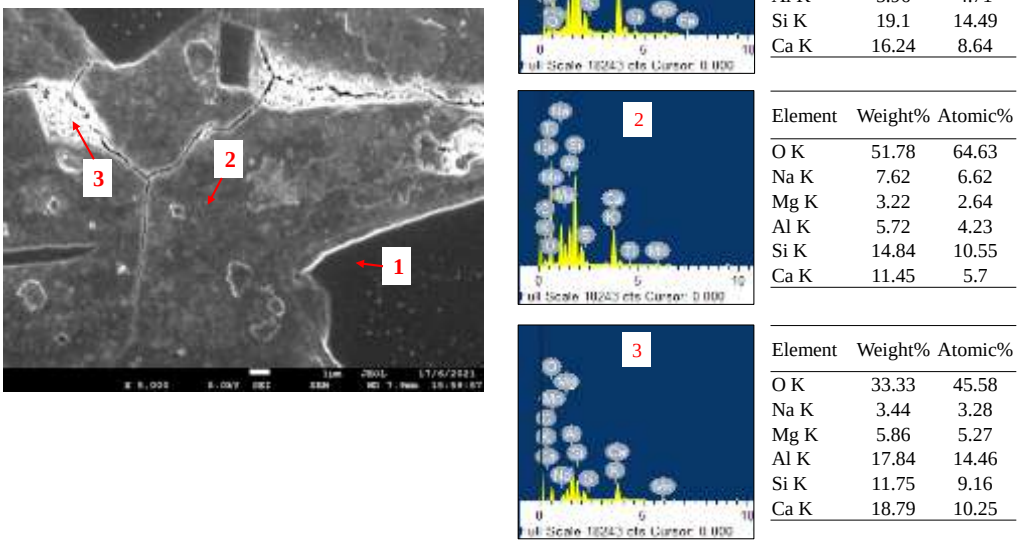

Element	Weight%	Atomic%
O K	48.05	64.03
Na K	0.55	0.51
Mg K	4.2	3.68
Al K	5.96	4.71
Si K	19.1	14.49
Ca K	16.24	8.64

Element	Weight%	Atomic%
O K	51.78	64.63
Na K	7.62	6.62
Mg K	3.22	2.64
Al K	5.72	4.23
Si K	14.84	10.55
Ca K	11.45	5.7

Element	Weight%	Atomic%
O K	33.33	45.58
Na K	3.44	3.28
Mg K	5.86	5.27
Al K	17.84	14.46
Si K	11.75	9.16
Ca K	18.79	10.25

Fig. 23. EDS spectrum and elemental analysis at different points of 10Mg5Mk.

3.9 Reaction Mechanism

In this study, slag-based sodium carbonate-activated mixes were produced by activating 10% of NC by weight. Even though low pH values were obtained at early stages (i.e. 12.3) in 100S, high strength values could be achieved due to the acceleration effect provided the moderately high-temperature curing at 60°C. Slag dissolution commenced when the pH value exceeded ~12 [18]. In 100S mixes, the reaction proceeded as a typical NC-activated system, in which a

preferential reaction occurred between Ca^{2+} from slag and CO_3^{2-} from NC, eventually forming calcite and gaylussite [17]. The reaction proceeded gradually due to the slow dissolution of slag under the lower pH induced by NC. Once the CO_3^{2-} was exhausted, the reaction rate expedited and phases such as hydrotalcite, Al incorporated C-(A)-S-H, and calcite formed as the main hydration products. With the incorporation of Mg^{2+} ions into the systems by reactive MgO substitution (10Mg mixes), the reaction was accelerated, and was associated with the increased formation of strength-providing hydrotalcite. While the hydration products were the same with 100S, higher hydrotalcite and periclase contents were observed due to the increased amount of available Mg ions in the system.

Alkali activation of metakaolin occurs in a different way than slag. The Glukhovsky model explained the mechanism of conjoined destruction reactions–coagulation–condensation–crystallization [100]. In the model, the first step consists of a breakdown of the covalent Si–O–Si and Al–O–Si bonds, which occurs when the pH of the alkaline solution rises. Then, an accumulation of the destroyed products occurs, which interacts among them to form a coagulated structure, leading to the generation of a condensed structure and crystallization [40]. An alkaline attack on the metakaolin results in silicate and aluminate species being released into the solution, with 5- and 6-coordinated Al being converted to 4-coordination upon dissolution [101]. It has been proposed that the initial release of Al may be more rapid than that of Si [102]. The dissolved Al may react with silicate, initially supplied by the activating solution, leading to the formation of aluminosilicate oligomers, which is why sodium silicate solutions are preferred as activators. Later on, the N–(A)–S–H gel develops and eventually begins to crystallize to form zeolites [103]. In this study, only sodium carbonate was used as an alkaline activator, which does not supply silicate.

The incorporation of a low amount of metakaolin into the system (10Mg5Mk mixes) made higher levels of aluminate and silicate species available. In this case, both types of reaction products, C-S-H or C-(A)-S-H from slag, hydrotalcite ($Mg_6Al_2(CO_3)(OH)_{16}.4(H_2O)$) with the Mg and Al substitution and aluminosilicate network, Na and Al-enriched C-(N,A)-S-H gel from metakaolin, could coexist, which resulted in slightly higher strength and better carbonation performance. The interaction of the precursors was also evident from the calorimetric measurements (Fig. 3), indicating the acceleration of the condensation reaction and the higher heat flow values obtained by blending slag, reactive MgO and metakaolin, which was associated with the increased dissolution of the precursors.

In the presence of higher amounts of metakaolin (5Mg10Mk mixes), the reaction was affected inversely. These samples revealed very low strength values (about 1 MPa) at all ages despite applying a moderately high curing temperature. It is well known that the availability of aluminum plays a key role in determining the properties of geopolymers [4,104]. Bernal et al. [41] investigated the structural evolution of alkali silicate-activated slag/metakaolin pastes and showed that the addition of metakaolin led to an increase in the total setting time, reduced the heat release and inversely affected the reaction mechanism by introducing a large quantity of additional Al [105]. De Silva et al. [106] studied the early-age reaction kinetics of metakaolin/sodium silicate/NaOH system and found that increasing Al led to lower strengths with increasing Na–Al–Si grained rather than amorphous Na–Al–Si phases in the mixes. In this study, 5Mg10Mk mix revealed the highest Al value due to the presence of metakaolin. Buchwald et al. [42] investigated the NH-activated metakaolin/slag blends, where higher activator concentrations were used for higher metakaolin-containing mixes to reach a constant Na/Al value of 0.4. In this study, the same NC concentration was used for all mixes. In addition, lower alkalinity (Fig. 4) might have inversely affected the reaction. Due to the different ratios of precursors and constant activator concentration, the Na_2O% of 5Mg10Mk was slightly lower, which could cause a reduction in the activation rate. Moreover, a very slow reaction mechanism

can be seen from isothermal calorimetry results (Fig 3). While other mixes reached their maximum heat flow at about 5 hours, for 5Mg10Mk, heat release started at 10 hours and achieved the maximum at about 20 hours. XRD results also corroborated the amorphous structure of 5Mg10Mk.

Considering the low alkalinity, higher Al concentrations and absence of additional silicate sources in 5Mg10Mk, any strength-providing phase could not be formed at early or later ages. Due to the low alkalinity, slag could not be dissolved enough initially, Ca^{2+} and Si^{4+} ions could not be released into the medium, and the high amount of free Al from metakaolin could not be involved in the formation of any hydration product. Therefore, even the use of higher temperatures during the curing process did not enhance the reaction mechanisms, resulting in the formation of only carbonate-containing phases such as calcite, periclase, and magnesite (Fig. 7).

4. Conclusions

This study investigated the performance and carbonation resistance of sodium carbonate-activated slag-based systems incorporating reactive MgO and metakaolin. The possible use of reactive MgO and metakaolin to enhance compressive strength and carbonation resistance was examined and their roles on the hydration mechanisms, compressive strength, microstructure and carbonation resistance were explored. A comprehensive analysis involving X-ray diffraction analysis (XRD), Fourier transform infrared spectrometry (FTIR), ^{29}Si and ^{27}Al solid-state nuclear magnetic resonance (NMR), and thermogravimetry-differential thermogravimetry (TG-DTG) was performed to clarify the hydration mechanism under environmental and accelerated carbonation conditions. Microstructural investigations were performed on paste samples, while compressive strength and carbonation resistance was investigated on mortar samples. Based on the results obtained, the following conclusions were drawn:

- Substitution of slag with Mg and Mk at 10% and 5% by weight slightly enhanced early age compressive strength development, revealing strengths higher than NC-activated mixes and PC-based mixes. The higher strength was attributed to the formation of hydrotalcite, C-(A)-S-H and C-(N,A)-S-H due to Mg, Al and Si provided by Mg and Mk.

- Mixes containing 5% Mg and 10% Mk, 5Mg10Mk mixes presented the lowest compressive strengths amongst all mixes, which was associated with the lack of any reaction between the precursors due to the lower initial pH and high amount of Al ions present in the medium.

- The use of Mg and Mk enhanced the carbonation resistance. 10Mg and 10Mg5Mk mixes presented the highest compressive strength values amongst the carbonated mixes. This enhancement was associated with the increased presence of Mg, Si, Al ions from the secondary binders, resulting in the formation of hydrotalcite and Na- and Al-enriched binder phase C-(N,A)-S-H.

- Decalcification of C-(A)-S-H was prevented in mixes containing Mg and Mk, while this phenomenon caused a significant reduction in compressive strength in control mixes 100S.

Overall, the findings of this study demonstrated that the incorporation of small amounts of Mg and Mk with slag had a considerable influence on the early age strength and carbonation resistance of NC-activated slag-based systems. The use of Mg and Mk provided additional Mg, Al, and Si ions in the system, enabling the formation of strength-providing phases such as

hydrotalcite, C-(A)-S-H and C-(N,A)-S-H gel. The amount of Mk used in these mixes should be controlled to avoid any undesirable strength loss. The data presented in this study can play a key role in the design of sustainable and durable NC-activated slag-based systems and provide a roadmap for the development of alternative binder systems with improved mechanical performance and carbonation resistance.

Acknowledgment

This study was supported by the research grant of Yildiz Technical University Research Foundation, Turkey (Grant ID: FYL-2021-4129). The authors would like to acknowledge the KUMAS A.S. and AKCANSA Cement Company for supplying the materials. Cise Unluer was funded by The Royal Society (project ref: ICA\R1\201310). We would like to acknowledge the Centre of High Field NMR Spectroscopy and Imaging at Nanyang Technological University for the use of their facilities. Funding supports from Ministry of National Development, Singapore (CoT-V1-2020-1) and National Research Foundation Singapore (SinBerBEST) are greatly appreciated.

References

[1] K.L. Scrivener, R.J. Kirkpatrick, Innovation in use and research on cementitious material, Cem. Concr. Res. (2008). https://doi.org/10.1016/j.cemconres.2007.09.025.

[2] J.L. Provis, Geopolymers and other alkali activated materials: Why, how, and what?, Mater. Struct. Constr. 47 (2014) 11–25. https://doi.org/10.1617/s11527-013-0211-5.

[3] J. Davidovits, Geopolymers - Inorganic polymeric new materials, J. Therm. Anal. 37 (1991) 1633–1656. https://doi.org/10.1007/BF01912193.

[4] P. Duxson, A. Fernández-Jiménez, J.L. Provis, G.C. Lukey, A. Palomo, J.S.J. Van Deventer, Geopolymer technology: The current state of the art, J. Mater. Sci. 42 (2007) 2917–2933. https://doi.org/10.1007/s10853-006-0637-z.

[5] M.T. Palomo, A. Grutzeck, M. W. Blanco, Alkali activated fly ashes: A cement for future, Cem. Concr. Res. 29 (1999) 1323–1329.

[6] V.F.F. Barbosa, K.J.D. MacKenzie, Thermal behaviour of inorganic geopolymers and composites derived from sodium polysialate, Mater. Res. Bull. 38 (2003) 319–331. https://doi.org/10.1016/S0025-5408(02)01022-X.

[7] H. Xu, Geopolymerisation of Aluminosilicate Minerals, 15 (2002) 270.

[8] D. Hardjito, S.E. Wallah, D.M.J. Sumajouw, B.V. Rangan, On the Development of Fly Ash-Based Geopolymer Concrete, ACI Mater. J. 101 (2005) 467–472. https://doi.org/10.14359/13485.

[9] N.K. Lee, H.K. Lee, Setting and mechanical properties of alkali-activated fly ash/slag concrete manufactured at room temperature, Constr. Build. Mater. 47 (2013) 1201–1209. https://doi.org/10.1016/j.conbuildmat.2013.05.107.

[10] X.H. Yuan, W. Chen, Z.A. Lu, H. Chen, Shrinkage compensation of alkali-activated slag concrete and microstructural analysis, Constr. Build. Mater. 66 (2014) 422–428. https://doi.org/10.1016/j.conbuildmat.2014.05.085.

[11] O.A. Mohamed, A review of durability and strength characteristics of alkali-activated slag concrete, Materials (Basel). 12 (2019). https://doi.org/10.3390/ma12081198.

[12] O. Burciaga-Díaz, Parameters affecting the properties and microstructure of quicklime (CaO)- Activated slag cement pastes, Cem. Concr. Compos. 103 (2019) 104–111. https://doi.org/10.1016/j.cemconcomp.2019.05.002.

[13] N.T. Dung, T.J.N. Hooper, C. Unluer, Improving the carbonation resistance of Na2CO3-

activated slag mixes via the use of reactive MgO and nucleation seeding, Cem. Concr. Compos. 115 (2021) 103832. https://doi.org/10.1016/j.cemconcomp.2020.103832.
[14] S. Bernal, R. San Nicolas, J. Provis, J.S.J. van Deventer, Alkali-activated slag cements produced with a blended sodium carbonate / sodium silicate activator, Adv. Cem. Res. (2015) 1–12. https://doi.org/dx.doi.org/10.1680/adcr.15.00013.
[15] A. Fernández-Jiménez, J. Palomo, F. Puertas, Alkali-activated slag mortars: Mechanical strength behaviour, Cem. Concr. Res. 29 (1999) 1313–1321. https://doi.org/10.1016/S0008-8846(99)00154-4.
[16] S.D. Wang, K.L. Scrivener, P.L. Pratt, Factors affecting the strength of alkali-activated slag, Cem. Concr. Res. 24 (1994) 1033–1043. https://doi.org/10.1016/0008-8846(94)90026-4.
[17] S.A. Bernal, J.L. Provis, R.J. Myers, R. San Nicolas, J.S.J. van Deventer, Role of carbonates in the chemical evolution of sodium carbonate-activated slag binders, Mater. Struct. Constr. 48 (2015) 517–529. https://doi.org/10.1617/s11527-014-0412-6.
[18] X. Ke, S.A. Bernal, J.L. Provis, Controlling the reaction kinetics of sodium carbonate-activated slag cements using calcined layered double hydroxides, Cem. Concr. Res. 81 (2016) 24–37. https://doi.org/10.1016/j.cemconres.2015.11.012.
[19] B. Akturk, A.B. Kizilkanat, N. Kabay, Effect of calcium hydroxide on fresh state behavior of sodium carbonate activated blast furnace slag pastes, Constr. Build. Mater. 212 (2019) 388–399. https://doi.org/10.1016/j.conbuildmat.2019.03.328.
[20] B. Akturk, S. Nayak, S. Das, A.B. Kizilkanat, Microstructure and strength development of sodium carbonate activated blast furnace slags, J. Mater. Civ. Eng. 31 (2019) 1–11. https://doi.org/10.1061/(ASCE)MT.1943-5533.0002944.
[21] C. Shi, P. V. Krivenko, D. Roy, Alkali-Activated Cements and Concretes, 2006.
[22] Y. Li, Y. Sun, Preliminary study on combined-alkali-slag paste materials, Cem. Concr. Res. 30 (2000) 963–966. https://doi.org/10.1016/S0008-8846(00)00269-6.
[23] A. Fernandez-Jimenez, F. Puertas, Effect of activator mix on the hydration and strength behaviour of alkali-activated slag cements, Adv. Cem. Res. 15 (2003) 129–136. https://doi.org/10.1680/adcr.15.3.129.36623.
[24] M. Kovtun, E.P. Kearsley, J. Shekhovtsova, Chemical acceleration of a neutral granulated blast-furnace slag activated by sodium carbonate, Cem. Concr. Res. 72 (2015) 1–9. https://doi.org/10.1016/j.cemconres.2015.02.014.
[25] U. Avila-López, J.M. Almanza-Robles, J.I. Escalante-García, Investigation of novel waste glass and limestone binders using statistical methods, Constr. Build. Mater. 82 (2015) 296–303. https://doi.org/10.1016/j.conbuildmat.2015.02.085.
[26] M. Zikmund, K. Putyera, K. Hrnčiarová, A novel route for the preparation of hydrotalcite and synthesis of intercalated reversible dioxygen-carrying cobalt(II) complexes, Chem. Pap. 50 (1996) 262–270.
[27] R. Salomão, L.M. Milena, M.H. Wakamatsu, V.C. Pandolfelli, Hydrotalcite synthesis via co-precipitation reactions using MgO and Al(OH)3 precursors, Ceram. Int. 37 (2011) 3063–3070. https://doi.org/10.1016/j.ceramint.2011.05.034.
[28] F. Jin, K. Gu, A. Al-Tabbaa, Strength and hydration properties of reactive MgO-activated ground granulated blastfurnace slag paste, Cem. Concr. Compos. 57 (2015) 8–16. https://doi.org/10.1016/j.cemconcomp.2014.10.007.
[29] M.A.A. Sherir, K.M.A. Hossain, M. Lachemi, Self-healing and expansion characteristics of cementitious composites with high volume fly ash and MgO-type expansive agent, Constr. Build. Mater. 127 (2016) 80–92. https://doi.org/10.1016/j.conbuildmat.2016.09.125.
[30] S. Ruan, C. Unluer, Comparative life cycle assessment of reactive MgO and Portland cement production, J. Clean. Prod. 137 (2016) 258–273.

https://doi.org/10.1016/j.jclepro.2016.07.071.
[31] S. Ruan, E.H. Yang, C. Unluer, Production of reactive magnesia from desalination reject brine and its use as a binder, J. CO2 Util. 44 (2021) 101383. https://doi.org/10.1016/j.jcou.2020.101383.
[32] H. Dong, C. Unluer, E.H. Yang, A. Al-Tabbaa, Recovery of reactive MgO from reject brine via the addition of NaOH, Desalination. 429 (2018) 88–95. https://doi.org/10.1016/j.desal.2017.12.021.
[33] F. Jin, A. Al-Tabbaa, Strength and drying shrinkage of slag paste activated by sodium carbonate and reactive MgO, Constr. Build. Mater. 81 (2015) 58–65. https://doi.org/10.1016/j.conbuildmat.2015.01.082.
[34] F. Jin, K. Gu, A. Abdollahzadeh, A. Al-Tabbaa, Effects of Different Reactive MgOs on the Hydration of MgO-Activated GGBS Paste, J. Mater. Civ. Eng. 27 (2015) 1–9. https://doi.org/10.1061/(asce)mt.1943-5533.0001009.
[35] N.T. Dung, C. Unluer, Influence of nucleation seeding on the performance of carbonated MgO formulations, Cem. Concr. Compos. 83 (2017) 1–9. https://doi.org/10.1016/j.cemconcomp.2017.07.005.
[36] N.T. Dung, C. Unluer, Development of MgO concrete with enhanced hydration and carbonation mechanisms, Cem. Concr. Res. 103 (2018) 160–169. https://doi.org/10.1016/j.cemconres.2017.10.011.
[37] N.T. Dung, C. Unluer, Performance of reactive MgO concrete under increased CO2 dissolution, Cem. Concr. Res. 118 (2019) 92–101. https://doi.org/10.1016/j.cemconres.2019.02.007.
[38] N.T. Dung, T.J.N. Hooper, C. Unluer, Enhancing the performance of MgO-activated slag-fly ash mixes by accelerated carbonation, J. CO2 Util. 42 (2020) 101356. https://doi.org/10.1016/j.jcou.2020.101356.
[39] S.A. Bernal, R. San Nicolas, R.J. Myers, R.M. de Gutiérrez, F. Puertas, J.S.J. van Deventer, J.L. Provis, MgO content of slag controls phase evolution and structural changes induced by accelerated carbonation in alkali-activated binders, Cem. Concr. Res. 57 (2014) 33–43. https://doi.org/10.1016/j.cemconres.2013.12.003.
[40] C. Li, H. Sun, L. Li, A review: The comparison between alkali-activated slag (Si + Ca) and metakaolin (Si + Al) cements, Cem. Concr. Res. 40 (2010) 1341–1349. https://doi.org/10.1016/j.cemconres.2010.03.020.
[41] S.A. Bernal, J.L. Provis, V. Rose, R. Mejía De Gutierrez, Evolution of binder structure in sodium silicate-activated slag-metakaolin blends, Cem. Concr. Compos. 33 (2011) 46–54. https://doi.org/10.1016/j.cemconcomp.2010.09.004.
[42] A. Buchwald, H. Hilbig, C. Kaps, Alkali-activated metakaolin-slag blends - Performance and structure in dependence of their composition, J. Mater. Sci. 42 (2007) 3024–3032. https://doi.org/10.1007/s10853-006-0525-6.
[43] A. Buchwald, R. Tatarin, D. Stephan, Reaction progress of alkaline-activated metakaolin-ground granulated blast furnace slag blends, J. Mater. Sci. 44 (2009) 5609–5617. https://doi.org/10.1007/s10853-009-3790-3.
[44] S.A. Bernal, R.M. de Gutiérrez, J.L. Provis, Engineering and durability properties of concretes based on alkali-activated granulated blast furnace slag/metakaolin blends, Constr. Build. Mater. 33 (2012) 99–108. https://doi.org/10.1016/j.conbuildmat.2012.01.017.
[45] H. Peng, C. Cui, Z. Liu, C.S. Cai, Y. Liu, Synthesis and reaction mechanism of an alkali-activated metakaolin-slag composite system at room temperature, J. Mater. Civ. Eng. 31 (2019) 04018345. https://doi.org/10.1061/(asce)mt.1943-5533.0002558.
[46] H. Zhu, G. Liang, H. Li, Q. Wu, C. Zhang, Z. Yin, S. Hua, Insights to the sulfate resistance and microstructures of alkali-activated metakaolin/slag pastes, Appl. Clay Sci.

202 (2021) 105968. https://doi.org/10.1016/j.clay.2020.105968.
[47] J.S. Yip, C. K., Lukey, G. C., Provis, J. L., & Van Deventer, Effect of calcium silicate sources on geopolymerisation, Cem. Concr. Res. 38 (2008) 554–564.
[48] C.K. Yip, J.S.J. Van Deventer, Microanalysis of calcium silicate hydrate gel formed within a geopolymeric binder, J. Mater. Sci. 38 (2003) 3851–3860. https://doi.org/10.1023/A:1025904905176.
[49] C.K. Yip, G.C. Lukey, J.S.J. van Deventer, The coexistence of geopolymeric gel and calcium silicate hydrate at the early stage of alkaline activation, Cem. Concr. Res. 35 (2005) 1688–1697. https://doi.org/10.1016/j.cemconres.2004.10.042.
[50] T. Bakharev, Resistance of geopolymer materials to acid attack, Cem. Concr. Res. 35 (2005) 658–670. https://doi.org/10.1016/j.cemconres.2004.06.005.
[51] A. Allahverdi, F. Škvára, Sulfuric acid attack on hardened paste of geopolymer cements part 1. Mechanism of corrosion at relatively high concentrations, Ceram. - Silikaty. 49 (2005) 225–229.
[52] R.R. Lloyd, J.L. Provis, J.S.J. Van Deventer, Acid resistance of inorganic polymer binders. 1. Corrosion rate, Mater. Struct. Constr. 45 (2012) 1–14. https://doi.org/10.1617/s11527-011-9744-7.
[53] I. Ismail, S.A. Bernal, J.L. Provis, R. San Nicolas, D.G. Brice, A.R. Kilcullen, S. Hamdan, J.S.J. Van Deventer, Influence of fly ash on the water and chloride permeability of alkali-activated slag mortars and concretes, Constr. Build. Mater. 48 (2013) 1187–1201. https://doi.org/10.1016/j.conbuildmat.2013.07.106.
[54] N.K. Lee, K.T. Koh, G.H. An, G.S. Ryu, Influence of binder composition on the gel structure in alkali activated fly ash/slag pastes exposed to elevated temperatures, Ceram. Int. 43 (2017) 2471–2480. https://doi.org/10.1016/j.ceramint.2016.11.042.
[55] P.S. Deb, P. Nath, P.K. Sarker, The effects of ground granulated blast-furnace slag blending with fly ash and activator content on the workability and strength properties of geopolymer concrete cured at ambient temperature, Mater. Des. 62 (2014) 32–39. https://doi.org/10.1016/j.matdes.2014.05.001.
[56] N.K. Lee, H.K. Lee, Influence of the slag content on the chloride and sulfuric acid resistances of alkali-activated fly ash/slag paste, Cem. Concr. Compos. 72 (2016) 168–179. https://doi.org/10.1016/j.cemconcomp.2016.06.004.
[57] J. Ren, H. Sun, Q. Li, Z. Li, L. Ling, X. Zhang, Y. Wang, F. Xing, Experimental comparisons between one-part and normal (two-part) alkali-activated slag binders, Constr. Build. Mater. 309 (2021) 125177. https://doi.org/10.1016/j.conbuildmat.2021.125177.
[58] American Society for Testing and Materials, ASTM C1702-17, Standard Test Method for Measurement and Prediction of Heat of Hydration of Portland Cement Using Isothermal Conduction Calorimetry, ASTM Int. West Conshohocken, PA, 2017. (2017).
[59] ASTM C109, ASTM C109 / C109M-21, Standard Test Method for Compressive Strength of Hydraulic Cement Mortars (Using 2-in . or [50-mm] Cube Specimens) 1, ASTM Int. West Conshohocken, PA, 2021. (2021). https://doi.org/10.1520/C0109.
[60] R.K. Harris, E.D. Becker, S. Cabral De Menezes, R. Goodfellow, P. Granger, NMR nomenclature: Nuclear spin properties and conventions for chemical shifts (IUPAC Recommendations 2001), Pure Appl. Chem. 73 (2001) 1795–1818.
[61] R.E.H. and K.W.Z. R. K. Harris, E. D. Becker, S. M. Cabral de Menezes, P. Granger, Further conventions for NMR shielding and chemical shifts (IUPAC Recommendations 2008), Pure Appl. Chem. 80 (2008) 59–84.
[62] Z.G. and G.H. D. Massiot, F. Fayon, M. Capron, I. King, S. Le Calvé, B. Alonso, J.-O. Durand, B. Bujoli, Modelling one- and two-dimensional solid-state NMR spectra, Magn. Reson. Chem. 40 (2002) 70–76.

[63] C. Bignozzi, M. C., Manzi, S., Lancellotti, I., Kamseu, E., Barbieri, L., & Leonelli, Mix-design and characterization of alkali activated materials based on metakaolin and ladle slag, Appl. Clay Sci. 73 (2013) 78–85.
[64] T. Yang, H. Zhu, Z. Zhang, Influence of fly ash on the pore structure and shrinkage characteristics of metakaolin-based geopolymer pastes and mortars, Constr. Build. Mater. 153 (2017) 284–293. https://doi.org/10.1016/j.conbuildmat.2017.05.067.
[65] A. Fernández-Jiménez, M. Monzó, M. Vicent, A. Barba, A. Palomo, Alkaline activation of metakaolin–fly ash mixtures: obtain of zeoceramics and zeocements, Microporous Mesoporous Mater. 108 (2008) 41–49. https://doi.org/https://doi.org/10.1016/j.micromeso.2007.03.024.
[66] S.A. Bernal, R. de Gutierrez, J. Provis, V. Rose, Effect of silicate modulus and metakaolin incorporation on the carbonation of alkali silicate-activated slags, Cem. Concr. Res. 40 (2010) 898–907. https://doi.org/https://doi.org/10.1016/j.cemconres.2010.02.003.
[67] C.K. Yip, G. Lukey, J.L. Provis, J.S.J. van Deventer, Effect of calcium silicate sources on geopolymerisation, Cem. Concr. Res. 38 (2008) 554–564. https://doi.org/10.1016/j.cemconres.2007.11.001.
[68] K. Steveson, M., & Sagoe-Crentsil, Relationships between composition, structure and strength of inorganic polymers, J. Mater. Sci. 40 (2005) 2023–2036.
[69] J. Deja, Carbonation aspects of alkali activated slag mortars and concretes, Silic. Ind. 3–4 (2002) 37–42.
[70] P. Yu, R.J. Kirkpatrick, B. Poe, P.F. McMillan, X. Cong, Structure of Calcium Silicate Hydrate (C-S-H): Near-, Mid-, and Far-Infrared Spectroscopy, J. Am. Ceram. Soc. 82 (2004) 742–748. https://doi.org/10.1111/j.1151-2916.1999.tb01826.x.
[71] I. García-Lodeiro, A. Fernández-Jiménez, M.T. Blanco, A. Palomo, FTIR study of the sol–gel synthesis of cementitious gels: C–S–H and N–A–S–H, J. Sol-Gel Sci. Technol. 45 (2007) 63–72. https://doi.org/10.1007/s10971-007-1643-6.
[72] B. Yuan, Q.L. Yu, H.J.H. Brouwers, Time-dependent characterization of Na2CO3 activated slag, Cem. Concr. Compos. 84 (2017) 188–197. https://doi.org/10.1016/j.cemconcomp.2017.09.005.
[73] M. Sitarz, M. Handke, W. Mozgawa, Identification of silicooxygen rings in SiO2 based on IR spectra, Spectrochim. Acta - Part A Mol. Biomol. Spectrosc. 56 (2000) 1819–1823. https://doi.org/10.1016/S1386-1425(00)00241-9.
[74] M. Sitarz, M. Handke, W. Mozgawa, E. Galuskin, I. Galuskina, The non-ring cations influence on silicooxygen ring vibrations, J. Mol. Struct. 555 (2000) 357–362. https://doi.org/10.1016/S0022-2860(00)00621-9.
[75] I. Lecomte, C. Henrist, M. Liégeois, F. Maseri, A. Rulmont, R. Cloots, (Micro)-structural comparison between geopolymers, alkali-activated slag cement and Portland cement, J. Eur. Ceram. Soc. 26 (2006) 3789–3797. https://doi.org/10.1016/j.jeurceramsoc.2005.12.021.
[76] I. García Lodeiro, D.E. Macphee, A. Palomo, A. Fernández-Jiménez, Effect of alkalis on fresh C-S-H gels. FTIR analysis, Cem. Concr. Res. 39 (2009) 147–153. https://doi.org/10.1016/j.cemconres.2009.01.003.
[77] G. Liu, M. Florea, H. Brouwers, Performance evaluation of sustainable high strength mortars incorporating high volume waste glass as binder, Constr. Build. Mater. 202 (2019) 574–588. https://doi.org/10.1016/j.conbuildmat.2018.12.110.
[78] Y.J. Zhang, Y.L. Zhao, H.H. Li, D.L. Xu, Structure characterization of hydration products generated by alkaline activation of granulated blast furnace slag, J. Mater. Sci. 43 (2008) 7141–7147. https://doi.org/10.1007/s10853-008-3028-9.
[79] F. Puertas, M. Palacios, T. Vázquez, Carbonation process of alkali-activated slag

mortars, J. Mater. Sci. 41 (2006) 3071–3082. https://doi.org/10.1007/s10853-005-1821-2.
[80] M. Palacios, F. Puertas, Effect of carbonation on alkali-activated slag paste, J. Am. Ceram. Soc. 89 (2006) 3211–3221. https://doi.org/10.1111/j.1551-2916.2006.01214.x.
[81] S.A. Bernal, E. Rodríguez, R.M. de Gutiérrez, V. Rose, F. Puertas, S. Delvasto, Carbonation behavior of mortar produced by alkali-activation of a granulated blast furnace slag, in: Proc. 23rd Int. Conf. Solid Waste Technol. Manag., Widener University, Philadelphia, PA, USA, 2008.
[82] H. Yang, R. Xu, X. Xue, F. Li, G. Li, Hybrid surfactant-templated mesoporous silica formed in ethanol and its application for heavy metal removal, J. Hazard. Mater. 152 (2008) 690–698. https://doi.org/10.1016/j.jhazmat.2007.07.060.
[83] S. Musić, N. Filipović-Vinceković, L. Sekovanić, Precipitation of amorphous SiO2 particles and their properties, Brazilian J. Chem. Eng. 28 (2011) 89–94. https://doi.org/10.1590/S0104-66322011000100011.
[84] B.S. Gebregziabiher, R. Thomas, S. Peethamparan, Very early-age reaction kinetics and microstructural development in alkali-activated slag, Cem. Concr. Compos. (2015). https://doi.org/10.1016/j.cemconcomp.2014.09.001.
[85] M.O. Yusuf, M.A.M. Johari, Z.A. Ahmad, M. Maslehuddin, Effects of addition of Al(OH)3 on the strength of alkaline activated ground blast furnace slag-ultrafine palm oil fuel ash (AAGU) based binder, Constr. Build. Mater. (2014). https://doi.org/10.1016/j.conbuildmat.2013.09.054.
[86] A. Abdalqader, F. Jin, A. Al-Tabbaa, Performance of magnesia-modified sodium carbonate-activated slag/fly ash concrete, Cem. Concr. Compos. 103 (2019) 160–174. https://doi.org/10.1016/j.cemconcomp.2019.05.007.
[87] Z. Shi, C. Shi, S. Wan, N. Li, Z. Zhang, Effect of alkali dosage and silicate modulus on carbonation of alkali-activated slag mortars, Cem. Concr. Res. 113 (2018) 55–64. https://doi.org/10.1016/j.cemconres.2018.07.005.
[88] K. Gu, F. Jin, A. Al-Tabbaa, B. Shi, J. Liu, Mechanical and hydration properties of ground granulated blastfurnace slag pastes activated with MgO-CaO mixtures, Constr. Build. Mater. 69 (2014) 101–108. https://doi.org/10.1016/j.conbuildmat.2014.07.032.
[89] J.M. Richardson, J.J. Biernacki, P.E. Stutzman, D.P. Bentz, Stoichiometry of Slag Hydration with Calcium Hydroxide, J. Am. Ceram. Soc. (2010). https://doi.org/10.1111/j.1151-2916.2002.tb00197.x.
[90] J. Dweck, P.F. Ferreira da Silva, P.M. Büchler, F.K. Cartledge, Study by thermogravimetry of the evolution of ettringite phase during type II Portland cement hydration, J. Therm. Anal. Calorim. (2002). https://doi.org/10.1023/A:1019950126184.
[91] J. Schneider, M.A. Cincotto, H. Panepucci, 29Si and 27Al high-resolution NMR characterization of calcium silicate hydrate phases in activated blast-furnace slag pastes, Cem. Concr. Res. 31 (2001) 993–1001. https://doi.org/10.1016/S0008-8846(01)00530-0.
[92] S.D. Wang, K.L. Scrivener, 29Si and 27Al NMR study of alkali-activated slag, Cem. Concr. Res. 33 (2003) 769–774. https://doi.org/10.1016/S0008-8846(02)01044-X.
[93] P. Schilling, L. Butler, A. Roy, H. Eaton, 29Si and 27Al MAS-NMR of NaOH-activated blast-furnace slag, J. Am. Ceram. Soc. 77 (1994) 2363–2368. https://doi.org/10.1111/j.1151-2916.1994.tb04606.x.
[94] T.D. Nguyen, T.J.N. Hooper, C. Unluer, Accelerating the reaction kinetics and improving the performance of Na2CO3-activated GGBS mixes, Cem. Concr. Res. 126 (2019) 105927. https://doi.org/10.1016/j.cemconres.2019.105927.
[95] P. Perez-Cortes, J.I. Escalante-Garcia, Gel composition and molecular structure of alkali-activated metakaolin-limestone cements, Cem. Concr. Res. 137 (2020) 106211.

https://doi.org/10.1016/j.cemconres.2020.106211.
[96] G. Le Saoût, M. Ben Haha, F. Winnefeld, B. Lothenbach, Hydration degree of alkali-activated slags: A 29Si NMR study, J. Am. Ceram. Soc. (2011) 4541–4547. https://doi.org/https://doi.org/10.1111/j.1551-2916.2011.04828.x.
[97] R. Tänzer, A. Buchwald, D. Stephan, Effect of slag chemistry on the hydration of alkali-activated blast-furnace slag, Mater. Struct. Constr. 48 (2014) 629–641. https://doi.org/10.1617/s11527-014-0461-x.
[98] S.A. Bernal, J.L. Provis, B. Walkley, R. San Nicolas, J.D. Gehman, D.G. Brice, A.R. Kilcullen, P. Duxson, J.S.J. Van Deventer, Gel nanostructure in alkali-activated binders based on slag and fly ash, and effects of accelerated carbonation, Cem. Concr. Res. 53 (2013) 127–144. https://doi.org/10.1016/j.cemconres.2013.06.007.
[99] X. Liu, M. Zhang, L.T. Shao, Experimental study on sulfate rich-soil stabilization with geopolymer, J. Water Res. Arch. Eng. 16 (2018) 136–142.
[100] V. Glukhovsky, G. Rostovskaja, G. Rumyna, High strength slag-alkaline cements, in: Roceedings Seventh Int. Congr. Chem. Cem., 1980: pp. 164–168.
[101] P. Duxson, G.C. Lukey, F. Separovic, J.S.J. Van Deventer, Effect of alkali cations on aluminum incorporation in geopolymeric gels., Ind. Eng. Chem. Res. 44 (2005) 832–839.
[102] L. Weng, K. Sagoe-Crentsil, Dissolution processes, hydrolysis and condensation reactions during geopolymer synthesis: Part I-Low Si/Al ratio systems, J. Mater. Sci. 42 (2007) 2997–3006. https://doi.org/10.1007/s10853-006-0820-2.
[103] P. Duxson, S.W. Mallicoat, G.C. Lukey, W.M. Kriven, J.S.J. van Deventer, The effect of alkali and Si/Al ratio on the development of mechanical properties of metakaolin-based geopolymers, Colloids Surfaces A Physicochem. Eng. Asp. 292 (2007) 8–20. https://doi.org/10.1016/j.colsurfa.2006.05.044.
[104] A. Fernández-Jiménez, A. Palomo, I. Sobrados, J. Sanz, The role played by the reactive alumina content in the alkaline activation of fly ashes, Microporous Mesoporous Mater. 91 (2006) 111–119. https://doi.org/10.1016/j.micromeso.2005.11.015.
[105] A.M. Rashad, Alkali-activated metakaolin: A short guide for civil Engineer-An overview, Constr. Build. Mater. 41 (2013) 751–765. https://doi.org/10.1016/j.conbuildmat.2012.12.030.
[106] A. Buchwald, H. Hilbig, C. Kaps, A.M. Rashad, A. Fernández-Jiménez, A. Palomo, I. Sobrados, J. Sanz, P. Duxson, S.W. Mallicoat, G.C. Lukey, W.M. Kriven, J.S.J. van Deventer, L. Weng, K. Sagoe-Crentsil, C. Li, H. Sun, L. Li, P. De Silva, K. Sagoe-Crenstil, V. Sirivivatnanon, Kinetics of geopolymerization: Role of Al2O3 and SiO2, J. Mater. Sci. 42 (2007) 2997–3006. https://doi.org/10.1016/j.micromeso.2005.11.015.